

## SHADOW, SCHLIEREN, AND INTERFEROMETER PHOTOGRAPHS AND THEIR USE IN BALLISTIC RANGES

Alvin Seiff

### 8.1 INTRODUCTION

Spark shadow photographs are the means most often used to record the instantaneous position and attitude of models in flight through ballistic ranges. It has long been known that such pictures also make visible certain features of the flow field about the projectile. This was demonstrated as early as the 1880's by Ernst and Ludwig Mach and by C.V. Boys in their famous photography of bullets in flight at low supersonic speeds<sup>8.1,8.2</sup>.

The ability of optical systems to make features of high speed gas flows visible has been invaluable in the history of fluid mechanics and the development of all kinds of devices to fly at high speeds in the atmosphere, from projectiles and missiles to aircraft and man-carrying spacecraft. Without the assistance provided by these pictures, our intuitive understanding of the nature of high speed flow would certainly be far less than it is today. It can properly be said that one of the key contributions of ballistic range studies has been the thousands of beautiful pictures of high speed flows they have provided.

Flow fields are made visible in photographs by virtue of the variations in the gas density, which result in variations in the refractive index. Light rays encountering the non-uniform medium are curved or bent, and hence intersect optical elements or the photographic film with altered directions or at altered locations. The velocity of light also is lowered in regions of high gas density compared to its value in the free stream. Different optical systems may be used to detect one or another of these effects of the flow field on the light rays and waves.

The three best known optical systems for this purpose are the shadowgraph, schlieren, and interferometer. Representative flow photographs recorded by these systems are shown in Figure 8.1\*. The qualities of flow visualization demonstrated in these examples are well and widely known. Shadowgraph pictures, such as Figure 8.1(a), display the bow shock wave as a dark band of finite width with a light band on its inner boundary. They also show secondary shock waves, such as the strong waves trailing the body; outlines of supersonic expansions, e.g. at the base corner of the cone; turbulence in boundary layers and wakes, showing fine details of structure; and weak disturbance waves generated either by body-fixed disturbances or the irregular edge of a turbulent boundary, as at the edge of the base flow in Figure 8.1(a). In schlieren photographs, such as Figure 8.1(b), regions of the flow field with uniform density gradient are brightened or darkened, depending on direction of the gradient and the knife edge orientation. Thus, in Figure 8.1(b), the shock wave outlines a dark region about the cone within which the density gradient normal to the knife edge is nearly uniform. Light intensity gradations occur in such pictures wherever there are density gradients, as in the region surrounding the wake where pressure pulses occur. The appearance of the turbulent wake is noticeably different from that in shadowgraphs, but close inspection reveals the same structural features. In interferograms, such as Figure 8.1(c), fields of dark and light interference fringes are displaced or shifted by the density distribution due to the flow. Discontinuities in fringe slope occur at shock waves, and fringes in other locations may be sharply curved (notably in the expansion fan in this picture). The fringe displacements measured may be quantitatively interpreted in terms of the density distribution of the flow field. Turbulent regions, such as the wake in Figure 8.1(c), give irregularity of contour to the fringes.

Although not usually thought of as a means of flow visualization, self-luminous photographs (e.g. Figure 8.2) of very high speed flow fields (velocity greater than about 6 km/sec) certainly contain information about the flow, and we mention them here for completeness. Such pictures can provide an outline of the high temperature shock layer, show the dimensions of the base flow region, and indicate the development of turbulence in the wake. The wake flow visualization occurs at the speed represented in Figure 8.2 because of the injection into the flow of efficient radiators by ablation of the polycarbonate plastic model. Pictures of this kind, whose flow visualization properties will not be further discussed herein, are obtained with image converter cameras or Kerr cell shuttered cameras (Chapter 6). The radiative properties of high speed flows are discussed in Chapter 9.

In this chapter, we will first discuss the three optical systems normally considered for flow visualization, and the principles by which flow features are made visible. The nature of the images to be expected from particular flow configurations will be analyzed and compared with images observed, since understanding how the image is formed permits us to be more precise and confident in our interpretations. The basis will be laid for quantitative consideration where it is desired. Some remarks on the capabilities and limitations of the three systems in ballistic testing will be included. The second main topic will be a discussion of research uses of flow

\* Flow photographs in this chapter which are not otherwise credited were obtained in the ballistic test facilities of the NASA Ames Research Center and its predecessor, Ames Aeronautical Laboratory of NACA.

visualization. These may be put into three classes: (1) The definition of flow configurations (studies of fluid mechanics). (2) The correlation of flow features with observed aerodynamic and flight behavior. (3) The indirect determination of properties of the flow or flowing gases. The second and sometimes the third categories constitute use of flow visualization in support of other test objectives. The first and third may represent uses of flow visualization as the principal approach to investigation. The third category will perhaps be obscure until some examples are given later in the chapter.

## 8.2 THE SHADOWGRAPH

Shadowgraph systems are widely used in ballistic ranges because of their simplicity and the excellence of flow visualization which they can provide.

### 8.2.1 Optical Arrangements

The simplest shadowgraph optical system consists of a spark source, approximating a point source, and a sheet of film. The spark firing is timed so that the model shadow falls on the film and light rays traverse the surrounding flow field, as in Figure 8.3. Sensitivity of the shadowgraph is determined by the distance from the model to the film, which also affects the magnification due to the conical light field.

The requirement for short spark duration, in the sub-microsecond range to prevent blurring of the image due to motion, has been discussed in Chapter 6. This requirement, imposed basically to permit accurate measurements of model position, is one of the factors which has led to the excellence of ballistic range shadowgraphs\*. Since the gas velocities relative to the earth are equal to or smaller than model velocity, the flow configuration, including its small details such as turbulent eddies, are "stopped" along with the model. Thus, transient features of the flow are photographed in their instantaneous configuration, even in the simplest shadowgraph system, as long as the spark duration is short enough to stop model blur.

Some advantage is gained by collimating the light in shadowgraph systems. The model shadow is then recorded in true size (except for diffraction effects), and distortions due to yaw are avoided. (The latter arise in conical light fields when the model axis is not a uniform distance from the film plane, in which case the magnification is a function of position along the model axis). A single spherical or parabolic mirror will produce a nearly-parallel beam of light which can be passed through a test region to fall on the recording film, arranged as in Figure 8.4. The shadowgraph sensitivity depends, as before, on distance from the flow disturbance to the film, but the collimating mirror may be placed at any convenient distance from the flight path without any first order effects on sensitivity and magnification. It should be noted, however, that imperfections of the collimating mirror and the off-axis arrangement of the spark can affect the accuracy of position measurements, since a perfectly parallel light column is not practically attainable.

If an imaging mirror is added to this arrangement on the film side of the test section, the system is called a focused shadowgraph system (Figure 8.5). The film is now effectively located at its image plane (as indicated in the sketch), and the sensitivity of the shadowgraph may be varied by moving this position toward or away from the flight path of the model projectile. This is conveniently accomplished by moving the film plane toward or away from the imaging mirror. The shadowgraph can be adjusted for minimum sensitivity by placing the effective film location on the flight path. The sensitivity will not then be zero, however, because refraction occurs as the light rays both approach and leave the plane of flight, within the bow shock wave envelope. The plane of focus may even be placed on the far side of the model from the imaging mirror - an arrangement impossible except in focused systems. This reverses the direction of light displacements in the picture.

Shadowgraphs of a blunt body with various sensitivity settings are compared in Figure 8.6. Increasing the sensitivity broadens the shock wave image and makes visible some features not discernible at the minimum setting, specifically the trailing shock wave and base flow. At the highest setting, the bow shock wave image is wider than the shock layer, and it obscures the model front face. Thus, the sensitivity appropriate for one region may be inappropriate for another, and the proper setting depends on the flow feature of immediate interest.

The value of focused shadowgraphs for rejecting model and flow field luminosity has been noted earlier in Chapter 6. An aperture plate which blocks extraneous light at the focal plane of the second mirror is a particularly effective addition (Figure 8.5). The overall rejection ratio of such systems for light from the flow field can be as large as  $10^4$  compared to that which would fall on a photographic plate placed in the usual position near the flight path. A very mild illustration of this effectiveness has been included in Figure 8.6. The two focused shadowgraph pictures are clear, while the parallel light, unfocused picture is fog exposed, even though the test relative velocity was only 11,000 ft/sec, and the luminosity was limited to the stagnation region of the spherical nose. With blunter models at higher speeds, the parallel light picture would become blackened and the model shadow indiscernible.

In the progression of optical systems, described above, it is evident that the schlieren system is the next step, requiring only the addition of a knife edge at the focal point of the imaging mirror. Discussion of this optical system will be deferred until after a consideration of the theory of shadowgraph systems.

---

\* By comparison, it was at one time conventional to use light sources of millisecond duration for flow photographs in wind tunnels.

### 8.2.2 Theory

A consideration of the processes by which light rays are redirected in compressible flow fields enables us to understand what we see in flow photographs, and opens the possibility of making quantitative interpretations. While we do not intend a comprehensive treatment of this subject, it will be of interest to describe quantitatively the effect of shock waves on light rays, and to write the equation governing the effect of regions of continuous but varying density. Consideration of these two topics provides the basis for understanding the images seen in shadowgraphs of shock waves, wakes, turbulence, boundary layers, separated flow boundaries, expansion-fan boundaries, streamlines of density-gradient discontinuity, and boundary-layer-induced sound or pressure fields - in short, all the phenomena normally displayed in shadowgraphs.

#### 8.2.2.1 Shadowgraph Images of Shock Waves

The index of refraction, like the more familiar fluid properties, density, pressure, and temperature, is discontinuous at a shock wave because the density is discontinuous. Light rays intersecting the wave surface therefore behave as they do at the surface of a lens, i.e., they obey Snell's law,

$$\frac{\sin i}{\sin r} = \frac{c_1}{c_2}, \quad (8.1)$$

where  $c_2$ , the speed of light within the shock layer, is slightly lower than  $c_1$ , the speed of light in the ambient atmosphere. The incident ray, where it is not normal to the shock surface, is therefore bent toward the normal on entering the disturbed flow field, and away from it on leaving (Figure 8.7), in both cases being deviated inward. Consequently, it intersects the shadowgraph film inward of its undisturbed location. Even this limited consideration is consistent with the shadowgraph image pattern typical of a shock wave, which is a dark (unexposed) band at the wave surface, with a brighter than normal band inside that (Figure 8.1a). The tangent ray (outermost boundary of the dark band) is not disturbed by the presence of the shock wave, except for diffraction effects. It therefore defines the location of the shock wave in space.

Let us now show that the presence of the dark and light bands can be fully predicted from elementary considerations, and derive expressions relating the width of the dark band to the strength of the shock wave. Consider an axially symmetric shock wave, shown in cross section in Figure 8.7 which, for simplicity, is assumed to be approximately cylindrical in the direction of flight so that all light rays lie and remain in the plane of the sketch. (Note that the equations written under this assumption apply exactly to a body of revolution in the plane of symmetry containing the incident ray direction, as well as to all spanwise stations of a cylinder in cross flow in a wind tunnel test). A further assumption is that the gas has uniform index of refraction within the shock layer. This assumption is made to isolate the effect of the shock wave alone on the light ray.

If we denote the deflection of the light ray at entry into the shock layer by  $\delta_1$ , then

$$i_1 = r_1 + \delta_1, \quad (8.2)$$

and  $\delta_1$  is presumed small. The complement of  $i_1$  is  $\epsilon_1$  and Equation (1) may be written

$$\frac{\cos(\epsilon_1 + \delta_1)}{\cos \epsilon_1} = \frac{c_2}{c_1}. \quad (8.3)$$

For non-ionized gases of constant composition, the speed of light may be related to the gas density through the expression

$$\zeta^{-1} = c/c_0 = 1 - G\rho, \quad (8.4)$$

where  $\zeta$  is the index of refraction,  $c_0$  is the speed of light in vacuum, and  $G$  is called the refractivity or the Gladstone-Dale coefficient\*. Its value for undissociated air is  $0.227 \text{ cm}^3/\text{gm}$ . Since  $G\rho \ll 1$ ,

$$c_2/c_1 = 1 - G(\rho_2 - \rho_1). \quad (8.5)$$

On expanding  $\cos(\epsilon_1 + \delta_1)$  and combining Eqs. (8.3) and (8.5), we obtain

$$\cos \delta_1 - \tan \epsilon_1 \sin \delta_1 = 1 - G(\rho_2 - \rho_1). \quad (8.6)$$

With small angle approximations for  $\delta_1$ , this may be solved to give

$$\frac{\delta_1}{\delta_{1t}} = -\frac{\tan \epsilon_1}{\delta_{1t}} + \left[ \left( \frac{\tan \epsilon_1}{\delta_{1t}} \right)^2 + 1 \right]^{\frac{1}{2}}, \quad (8.7)$$

\* For ionized gases,  $c/c_0 = 1 - \alpha \lambda^2 n_e - G\rho$ , where  $n_e$  is the electron number density,  $\lambda$  is the light wavelength, and  $\alpha$  is a coefficient. At appreciable degrees of ionization, the change in the velocity of light due to free electrons tends predominate over that due to neutral gas particles. In such a case, with monochromatic light, Equation (8.7) will apply, but Equation (8.8) must be modified to read  $\delta_{1t} = [2(\alpha \lambda^2 n_e - G\rho_1)]^{\frac{1}{2}}$ .

where  $\delta_{it}$  is the deflection angle for grazing incidence ( $\epsilon_1 = 0$ ),

$$\delta_{it} = [2G\rho_1(\rho_2/\rho_1 - 1)]^{\frac{1}{2}}. \quad (8.8)$$

and  $\delta_1/\delta_{it} \rightarrow 0$  as  $(\tan \epsilon_1)/\delta_{it} \gg 1$ .

Equations (8.7) and (8.8) relate the ray deflection angle on entry into the shock layer to the complement of the incidence angle  $\epsilon_1$ , the ambient density  $\rho_1$ , and the shock strength as measured by the density ratio  $\rho_2/\rho_1$ . From symmetry,  $i_2 = r_1$ , and from Equation (8.1), it can readily be shown that the ray deflection on leaving the shock layer is equal to that on entering. Hence, the total angular deflection of the light ray, neglecting the refraction that occurs inside the shock layer, is twice the value given by Equations (8.7) and (8.8).

$$\delta = 2\delta_1. \quad (8.9)$$

The linear deflection of the ray on the shadowgraph film, designated  $\Delta n$  in Figure 8.7, is just

$$\Delta n = B\delta. \quad (8.10)$$

for a distance  $B$  from the model to the film plane\*. If we define the coordinate  $n$  to be zero at the projected actual position of the shock wave, then a light ray which would have intersected the film at  $n$  now falls instead at

$$n_f = n + \Delta n = n + B\delta(n). \quad (8.11)$$

The coordinate  $n$  is related to the complement of the incidence angle  $\epsilon_1$ , as may be seen from Figure 8.7, by

$$\cos \epsilon_1 = 1 - n/R. \quad (8.12)$$

Equations (8.7) through (8.12) allow  $n_f$  to be calculated for all  $n$ . A representative example is given in the lower part of Figure 8.8. The dark band is predicted by these equations and is calculated for this example to be 2.5 mm wide, starting at the projected actual position of the shock wave,  $n_f = 0$ . Note that light intersecting the shock wave in the first few thousandths of a mm inside the tangent ray is directed 18.7 mm inside the flow field in the shadowgraph.

Normal or uniform exposure of the film is defined by the total energy per unit film area,  $E$ , provided by the light pulse from the shadowgraph spark. Outside the disturbed flow field, the energy falling on unit width of the film in elemental length  $\Delta n$  is  $E\Delta n$ . For rays originally separated by  $\Delta n$  which pass through the shock wave, their spacing on the film may be termed  $\Delta n_f$ , and the energy per unit area is  $E(\Delta n/\Delta n_f)$ . The ratio of this energy to the uniform energy per unit area is just  $\Delta n/\Delta n_f$ , which will be termed the average light amplification factor  $\bar{A}$  over the zone  $\Delta n_f$ .

Since, as may be seen in Figures 8.8 and 8.9, there are two contributions to light intersecting the film at given  $n_f$ , one originating in the dark band and one outside it,  $\Delta n$  is the sum of two parts. For positive  $\Delta n_f$ ,  $\Delta n_1$  is negative (see Figure 8.8) and  $\Delta n_2$  is positive, but both contribute positively to the exposure of the film, so we write

$$\bar{A} = \frac{-\Delta n_1 + \Delta n_2}{\Delta n_f}. \quad (8.13)$$

In the limit of very small  $\Delta n_f$ , the amplification factor at a point becomes

$$A = -dn_1/dn_f + dn_2/dn_f. \quad (8.14)$$

At the outer boundary of the light band, slopes and amplification factor become locally infinite†. Amplification factors for the example are plotted in the upper part of Figure 8.8. The bright region with  $A > 2$  is a band 0.3 mm wide, beyond which  $A$  levels off to a value of about 1.5. A shadowgraph picture taken at approximately the conditions of the example is reproduced in Figure 8.10. The dark band on the axis of symmetry measures 2.6 mm wide on the original negative.

The above analysis is purposely simplified to give insight into the shock wave image-forming process. It is, however, a first order quantitative description of that process in shadowgraphs.

### 8.2.2.2 Refraction Within the Shock Layer

Now let us turn attention to refraction effects within the shock layer, and derive the governing equations. Then we will give a phenomenological discussion of images of flow features frequently visible in shadowgraph pictures, and how they are formed.

\* Note in Figure 8.7 that the effective position of the model differs slightly from the actual position, being defined by the point of intersection of the extended incident ray with the extended emergent ray.

† Total light on the film remains finite, however, because infinite amplification occurs only along a line of zero width.

A wave front, proceeding along  $z$  across a region in which density and hence light velocity varies along  $y$ , will rotate, as indicated schematically in Figure 8.11, where  $yz$  has been chosen as the plane containing the light ray and the density gradient. Since the velocity  $c_2$  is greater than  $c_1$ , the upper end of the wave front advances in time  $\Delta t$  by a distance  $z_2 > z_1$ , and rotates by an amount

$$\Delta\theta = \frac{\Delta z}{\Delta y}, \quad (8.15)$$

where

$$\Delta z = (c_2 - c_1)\Delta t = z_1 \left( \frac{\zeta_1}{\zeta_2} - 1 \right), \quad (8.16)$$

and  $\zeta_1$  and  $\zeta_2$  are the local refractive indices. Since  $\Delta\zeta = \zeta_2 - \zeta_1$ ,

$$\Delta z = -z_1 \frac{\Delta\zeta}{\zeta_2} \quad (8.17)$$

and

$$\Delta\theta = -\frac{z_1}{\zeta_2} \frac{\Delta\zeta}{\Delta y} \quad (8.18)$$

In the limit of vanishing  $\Delta t$ , for which  $z_1$  becomes infinitesimal, and for vanishing  $\Delta y$ , Equation (8.18) becomes the differential equation

$$\frac{\partial\theta}{\partial z} = -\frac{1}{\zeta} \frac{\partial\zeta}{\partial y}. \quad (8.19)$$

The rate of ray rotation along the direction of propagation is thus proportional to that component of the gradient of the index of refraction which is normal to the ray. Since  $R_c d\theta = dz$ , where  $R_c$  is the radius of curvature of the ray, we identify  $\partial\theta/\partial z$  as  $1/R_c$ . The total rotation of a ray traversing the density field is obtained by integration of Equation (8.19) over  $z$ , where  $z$  is a curvilinear coordinate following the ray and  $y$  remains perpendicular to  $z$ . The angle of the ray at exit from the field is

$$\theta_e = \int_0^{\theta_e} d\theta = -\int_{z_i}^{z_f} \frac{1}{\zeta} \frac{\partial\zeta}{\partial y} dz \quad (8.20)$$

A bundle of rays, within which  $\theta_e$  is constant will deliver the same energy intensity to the film as if it had been undeviated. Only where

$$\frac{\partial\theta_e}{\partial y} \neq 0 \quad (8.21)$$

is the exposure affected. Differentiation of Equation (8.20) yields

$$\frac{\partial\theta_e}{\partial y} = \int_{z_i}^{z_f} \left[ \frac{1}{\zeta^2} \left( \frac{\partial\zeta}{\partial y} \right)^2 - \frac{1}{\zeta} \frac{\partial^2\zeta}{\partial y^2} \right] dz + \frac{1}{\zeta_i} \left( \frac{\partial\zeta}{\partial y} \right)_i \frac{\partial z_i}{\partial y} - \frac{1}{\zeta_f} \left( \frac{\partial\zeta}{\partial y} \right)_f \frac{\partial z_f}{\partial y}. \quad (8.22)$$

By use of Equation (8.4), this may be expressed in terms of the gas density,

$$\frac{\partial\theta_e}{\partial y} = \int_{z_i}^{z_f} \left[ G^2 (1 - 2G\rho) \left( \frac{\partial\rho}{\partial y} \right)^2 - G(1 - G\rho) \frac{\partial^2\rho}{\partial y^2} \right] dz + G(1 - G\rho_i) \left( \frac{\partial\rho}{\partial y} \right)_i \frac{\partial z_i}{\partial y} - G(1 - G\rho_f) \left( \frac{\partial\rho}{\partial y} \right)_f \frac{\partial z_f}{\partial y} \quad (8.23)$$

Thus,  $\partial\theta_e/\partial y$  depends on both first and second derivatives of density taken normal to the ray.

Exposure intensity on the film in a region between two rays, initially a distance  $dy$  apart, whose emergent angles differ by  $d\theta_e$ , depends on the separation with which they intersect the film,  $dy + Bd\theta_e$ . The local light amplification factor  $A$  may be expressed as

$$A = \frac{dy}{dy + Bd\theta_e} = \frac{1}{1 + B\partial\theta_e/\partial y} \quad (8.24)$$

Thus, when  $\partial\theta_e/\partial y$  is negative, the rays are convergent and  $A > 1$ . With  $\partial\theta_e/\partial y$  positive, the rays are divergent and  $A < 1$ .

### 8.2.2.3 Shadowgraph Images of Particular Flow Features

Ordinarily, in viewing shadowgraph pictures, we are less concerned with subtle variations in the light amplification factor than in the appearance of sharply delineated photographic features which arise where  $\theta_e$  undergoes discontinuous or nearly discontinuous change. Let us now consider in a more qualitative way the nature of such interactions of the light field with particular density fields, specifically Prandtl-Meyer expansions, turbulent eddies, streamlines of density-gradient discontinuity, and laminar boundary layers.

In Prandtl-Meyer expansions, density is constant on Mach lines emanating from the expansion corner. A density gradient exists normal to those lines. The expansion fan is bounded by an initial Mach line, inclined at the initial Mach angle to the streamlines approaching the corner, and a final Mach line, inclined at the final Mach angle to the streamlines leaving the expansion. The gradient is discontinuous at the initial Mach line and at the final Mach line, so that the density distribution is of the type schematically indicated in Figure 8.12. The coordinate  $y$  lies along the direction of the density gradient, in the plane which is normal to the incident ray direction. The bending of the light rays by this density profile is schematically indicated. The disturbance is, for simplicity, collapsed to a plane, which may be regarded as its effective location, where the emergent rays extended backwards intersect the incident rays. Since the density gradients outside the expansion fan are presumed small by comparison with those within the fan, rays passing outside the fan are indicated as undeflected. Those passing through the fan are deflected toward the high density region. As a result, a doubly-exposed light band occurs along and outside the initial Mach line, while an unexposed or dark band lies along and inside the final Mach line. Since the light-ray deflection angles  $\theta_e$  vary comparatively slowly in the intervening region, the amplification factors,  $A$ , Equation (8.24), are near unity and the exposure is almost uniform. A shadowgraph in which an expansion fan originating at the model base corner may be compared with the above description has been given in Figure 8.1(a)\*.

Turbulence is recorded in shadowgraph systems as a collection of spot patterns whose size and shape show some degree of regularity. These spots may be clustered in large, seemingly random, groupings, giving an irregular outline to the boundary layer or wake (see, e.g., the wake of the model in Figure 8.1(a)), or in a single file row in the early stages of development of a turbulent layer (Figure 8.13). The mere fact that turbulence is visible in shadowgraphs, of course, is evidence of density fluctuations. If we assume that the eddy or vortex is a basic element of turbulent flow, then the fact that pressure forces must be centrally directed in a vortex to maintain circular motion, and that density will have the same direction of variation as pressure leads us to expect a density distribution in an idealized eddy like that indicated in Figure 8.14. The light field passing through this density pattern is deflected outward, yielding a bright ring around the eddy. Inside the bright ring, there will be a dark center, with perhaps a spot of light at the center, depending on the sharpness of the density minimum. The correspondence of this description with the spot patterns seen in Figure 8.13 may be regarded as evidence for the existence of such density patterns in the flow.

The density distribution across a representative laminar boundary layer on a ballistic range model is like that in Figure 8.15. The density rises near the wall because of cooling of the inner layers of the boundary layer by the model surface, which is generally at a much lower temperature than the boundary layer recovery temperature. As in the case of the turbulent eddy, the light field diverges on either side of the density minimum, some light being refracted into the model shadow. The divergent region is a region of dimmer than normal exposure. A band of convergent rays originates near the boundary layer edge, to produce a bright band which lies roughly along, but, depending on the shadowgraph sensitivity, possibly inside or outside the boundary layer edge. Thus the boundary layer image is expected to comprise a region of reduced exposure near the model surface and extending slightly inside it, with a bright band near the boundary layer edge†.

The existence of this pattern with attached laminar boundary layers is very difficult to determine, because of two factors. First, the boundary layers are generally very thin – typically a few thousandths of an inch thick. Second, wave diffraction patterns occur at the edge of the model shadow, and interfere with observation of the boundary layer image. However, separated laminar boundary layers are readily seen, as, e.g., at the boundary of the base flow region in Figure 8.16. Primarily, a single bright band is recorded, presumably the outward directed convergent rays of Figure 8.15.

Transition to turbulence can often be seen in following this line. The line develops irregularities and gaps before the spot patterns typical of eddies begin to appear. However, a high contrast line pattern behind the base is not always proof of laminar boundary layer coming off the base, since it has been observed that such lines occur for a short distance beyond separation of a turbulent boundary layer (see baseflow region in Figure 8.17). This may be the exposure intensification from inward directed light from the sublayer, which, behind the model base falls on an already illuminated region of the film. The dissipation of the bright line would then signify the disappearance of the sublayer, without a wall to bound it.

Streamwise vortices frequently occur in laminar boundary layers as an early stage of the transition to turbulence. When these occur in a base flow region, they might be expected to leave an image on the film. Since the density distribution in the vortex cross section is like that of Figure 8.14, extended along the length of the vortex, the image pattern should consist of two bright lines surrounding the darkened vortex core. Several patterns of this description can be seen in the base region of the cone in Figure 8.16, and are attributed to streamwise vortices.

\* An interesting but not typical feature of this picture is the large deflection which the light band takes near the expansion corner. This is attributed to combined effects of the boundary layer and the expansion.

† A similar discussion with similar conclusions has been given by Holder and North<sup>8,9</sup> (see their Figure II-26 and its discussion on page 28). They considered two-dimensional boundary layers with density profiles appropriate in wind tunnels at zero heat transfer – i.e., they do not exhibit the upturn near the wall.

When secondary shock waves intersect a bow shock wave, as in Figure 8.18, streamlines crossing the bow wave above and below the intersection experience different total pressure losses (entropy increases). Since, at the dividing streamline, there must exist a common static pressure, it can be demonstrated from elementary considerations that the velocity and temperature are discontinuous at this streamline. It follows from the gas law that density is discontinuous, being higher on the inward side. Light rays will interact with this density jump just as they do with a weak shock wave. Hence, in Figure 8.18, we see that the streamline originating at the wave intersection point near the conical tip is visible downstream, and has the dark outer band, light inner band typical of shock wave images. Because there is a high velocity gradient across this streamline, it develops into a shear layer which can become turbulent, as in Figure 8.18.

Figure 8.19 is a somewhat more subtle (and more typical) example of the wave intersection phenomenon, wherein a large number of streamlines become marked by the intersection with the bow wave of wavelets generated by disturbances fixed on the model surface. This method of marking the streamline paths can be very valuable in studies of the flow field.

It has also been observed that a very strong expansion interacting with a shock wave will mark a streamline<sup>8.4</sup>. In this case, while density is continuous, the density gradient is discontinuous. Characteristics solutions performed on a large-angled cone cylinder showed that, along Mach waves emanating from the base corner of the cone, the density distribution was of the type shown in Figure 8.20. The discontinuity in gradient occurred along the streamline crossing the bow wave at the point of intersection of the bow wave with the first Mach wave of the expansion. Light rays are deflected away from this streamline in both directions, leaving it marked as a dark band. This marking is observed to persist far downstream.

The above examples illustrate qualitative prediction of shadowgraph images, given the density distribution. When research objectives demand it, the predictions can be made quantitative.

#### 8.2.2.4 Dimensional Distortion in Shadowgraph Flow Fields

If dimensions of the flow field are to be measured from shadowgraphs, it is important to consider at least qualitatively the details of the process by which the image is formed so that possible distortions can be evaluated. Flow field dimensions which have been obtained from shadowgraphs in past research include shock wave stand off distances, shock wave profiles, angles of embedded shock waves, convergence angles of wakes, angles of Mach wavelets from surface disturbances, initial and final Mach angles of expansion fans, thicknesses of turbulent boundary layers, thicknesses of wake minimum sections, and diameters of turbulent wakes far downstream. When primary research results depend on these measurements, it is important to evaluate the optical distortions, either inherent in producing the shadowgraph image of the feature being measured or in the surrounding flow. When large distortions are found to be present, it may be possible to correct the data from an optical analysis.

An example of large distortion may be of interest. In the course of some turbulent boundary layer studies, the writer desired to measure the boundary layer thickness from shadowgraphs of thin-walled tubes with sharp leading edges, having flow both inside and out (Figure 8.21). As a test for optical distortion, model image diameters were measured in the pictures. The model image diameters were found to be consistently larger than actual diameter, 3.8 cm, by as much as 0.25 cm. The measurements of boundary layer thickness therefore could not be accepted as valid, without considering the cause of the distortion and its effect.

It was known from previous calibrations that the light beams were accurately parallel, so simple magnification was not the cause. Pictures of stationary models in the test section showed that light diffraction (discussed below) caused an image enlargement of only about 0.05 cm. Analysis of light ray deflections at the shock wave and in the flow external to the boundary layer showed that they were opposite in direction and produced a net movement of the ray on the film of only a few thousandths of a cm in the vicinity of the model edge. Hence, none of these could explain the observed distortion. In the thick turbulent boundary layer, however, the density gradients were large near the wall, and the light path within the boundary layer on models of this diameter was long. By use of theoretical density profiles, refraction was estimated to cause outward ray displacement of 0.1 cm on each side of the body for rays passing just outside the temperature maximum near the model surface. Thus, the model diameter distortion was traced primarily to boundary layer refraction. Near the boundary layer edge, however, the mean density gradient was small, and the mean distortion calculated to be negligible. Hence, it was concluded that the most reliable measurement of boundary layer thickness was to be obtained by measuring the distance from the boundary layer edge on one side of the model to the boundary layer edge on the other side, and subtracting the actual model diameter. It should be pointed out that the distortion occurring in this example were larger than usual for turbulent boundary layers, for two reasons - because the boundary layers were very thick (artificially thickened by use of high drag trips); and because of the large model diameter.

Other quantitative uses of shadowgraph images are suggested by the theory, given earlier. One, which was proposed in Reference 8.5, is to determine the density ratio across a shock wave from the width of the dark band which it generates in the shadowgraph. It is evident that very accurate measurement and correction for diffraction effects would be required to give useful accuracy. Also suggested in that reference, but, to the writer's knowledge, untried in the intervening years, was the use of a wire grid of accurately known dimensions, superimposed on and photographed through a flow field to indicate ray angles induced by the flow field. These could be compared with predicted ray directions for confirmation of theoretical density distributions, or possibly used in an Abel-integral approach (see Interferometry) to deduce density profiles.

Other quantitative applications will suggest themselves to the interested investigator.

### 8.2.2.5 Diffraction Effects

The discussion of the theory and phenomenology of image formation in shadowgraph pictures would not be complete without some comments on diffraction effects. These occur at the model shadow edges, and at every sharp-edged dark band such as those indicated in Figures 8.12 and 8.20, as well as at the undeflected tangent ray at a shock wave surface. Diffraction, a wave interference phenomenon, produces fringe patterns at shadow edges in monochromatic light (see, e.g., Reference 8.6, page 197). The first fringe is bright, and its center lies at a distance  $1.2(B\lambda/2)^{1/2}$  outside the edge of the geometric shadow, where  $B$  is the distance from the object to the film, and  $\lambda$  is the wavelength of the light. (For example, with  $\lambda = 5000 \text{ \AA}$  and  $B = 30 \text{ cm}$ , the distance to the fringe center is  $0.33 \text{ mm}$  outside the shadow edge). This bright fringe forms a border around the shadow, and diameters are naturally measured by the eye to its inner edge. Shadow images are accordingly found to be larger than the object, in perfectly parallel light.

In monochromatic light from a point source, a series of fringes would be observed, but in the multi-colored spectrum characteristic of a shadowgraph spark (Chapter 6), only the first bright fringe and the first dark fringe are usually seen, with an occasional suggestion of a second bright fringe. Typical of these patterns are those in Figure 8.22, photographed in a shadowgraph light beam with a razor blade and a thin-walled tubular model mounted on a supporting stand to serve as shadow forming objects. The first bright fringe seen around these stationary objects is the same kind of light pattern expected from a laminar boundary layer, and this similarity makes it difficult to distinguish one phenomenon from the other.

Theoretically, as noted above, one would expect fringes at the shadow edge caused by a shock wave or a density gradient discontinuity, and occasionally, in a print of suitable contrast, one can find a suggestion of a bright fringe at the appropriate edges of the dark band. Such fringes can be seen in original prints on Figures 8.10 and 8.13 at the outer edge of the bow shock wave dark band, and in Figure 8.16 at both edges of the final Mach wave of the base expansion fan. One should always keep diffraction effects in mind in studying and interpreting shadowgraph pictures, as they can be responsible for some of the subtler things seen, as well as for the easily measurable effect on apparent object diameters, even in the absence of flow.

## 8.3 SCHLIEREN SYSTEMS

Schlieren optical systems for flow visualization have been used far less extensively than shadowgraphs in ballistic ranges. Primarily, this is due to the excellence of flow visualization afforded by the simpler shadowgraphs under usual ballistic-range conditions. Schlieren systems require somewhat more care in their use, since the image of the light source must be carefully aligned on the knife edge, and the pictures obtained may seem, in some respects, less informative than shadowgraphs. The masses of dark and light exposure which differentiate expansion from compression regions tend to dominate the picture, while many interesting details, such as noise fields due to turbulence tend to be lost. However, it has been often assumed that in some circumstances, schlieren pictures may possess higher sensitivity to flow features than shadowgraphs.

Schlieren photography has thus found application in ballistic range studies of laminar wakes, far downstream of bodies flying through low density air, and in some other problems as well. We will therefore briefly review schlieren systems, with attention to optical arrangement and basis of operation.

### 8.3.1 Optical Arrangements

The standard optical arrangement for a parallel light schlieren system is shown in Figure 8.23. The film is so located that the model image formed by the second mirror is in focus at the film plane. Then light rays refracted by the flow field are, in the image plane, returned approximately to their original locations relative to the model. Ideally, this cancels the shadowgraph effect, but in practice, this is not fully achieved, since rays passing through different parts of the flow field do not have the same effective plane of origin. Also, even a small error in focal position due, e.g., to the model flying out of the bore sight plane, can result in a shadowgraph image of the shock waves.

The image of the spark light source formed by the second mirror is partly occulted on the knife edge, thereby dimming the level of illumination on the film. The knife edge does not shadow any part of the film, however, because rays from all parts of the source image fall on all parts of the film. The sensitivity of the schlieren system depends on the width of the source image which is allowed to pass the knife edge. The sensitivity is increased by reducing the unocculted width of the source image. It follows that the position of the source image on the knife edge is required to be either stable or adjusted just prior to use.

Stability may be hard to achieve because of earth movement, thermal expansion, etc. An added fundamental difficulty is that conventional spark light sources do not fire at a fixed location on the electrodes, but rather, the spark moves about, finding a new location at each firing. Mercury filled discharge lamps also exhibit this behaviour when fired in short duration pulses. Note in Figure 8.24, from Reference 8.7, the progressive change in shape of the mercury arc column over a sequence of 12 firings in 110 microseconds.

If the source movements due to all causes are appreciable compared to source diameter, the sensitivity variations will be large. The effect of uncontrolled source position is illustrated in Figure 8.25, which is a schlieren picture inadvertently obtained in a focused shadowgraph system. In this case, the source image, intended to be centered in a circular aperture, moved onto the edge of the aperture. A schlieren visualization of the wake resulted, while the bow shock wave and discontinuity streamlines are shadowgraph images. The high sensitivity of the schlieren system to changes in light ray angles is well demonstrated by the appearance of rings in the focusing mirror. For shadowgraph use, this mirror has no detectable imperfections.



To overcome the problem of source movement within the electrodes, confined sparks have been developed. Reference 8.3 describes four configurations of confined sparks which have been used in wind tunnel schlieren systems, and Reference 8.8 indicates "a semi-confined spark between parallel electrodes in a quartz block" used in a ballistic range application of schlieren photography. Sketches of these confined spark sources are given in Figure 8.26. The dimensions used in the semi-confined gap were approximately 0.5 mm width by 5 mm length. Light from the spark is imaged on a smaller slit, which further restricts source movement, since the slit becomes the schlieren source. For maximum sensitivity, slits of very small width (e.g., 0.1 mm) have been used.

Other schlieren optical arrangements than the parallel light system of Figure 8.23 are possible and have been used. A single mirror, single pass, conical light system is shown in Figure 8.27. While having the advantage of requiring only one parabolic mirror, this arrangement has two conspicuous disadvantages: (1) The source must be placed more than twice the focal distance from the mirror, to satisfy the requirement for source image location on the mirror side of the flight path. This means that the light falling on the mirror and hence on the film is much less than in Figure 8.23 for mirrors of equal focal length and aperture. (2) The mirror is required to be severalfold larger than the intended field of view. Thus, this arrangement is in need of a large aperture mirror of short focal length - i.e., an expensive mirror.

Double light pass systems have been used in cases where high sensitivity is required. The parallel light system may be made a double pass system by replacing the second parabolic mirror by a flat mirror, just slightly inclined (away from normal to its incident rays) so that the source image formed by the first mirror does not fall directly on the source. The first (collimating) mirror thus becomes the image forming mirror for both the source and the model. The tilting of the flat mirror gives rise to a slightly displaced second (double) image, which degrades picture quality. This can be partially avoided by aligning the flat mirror to return the source image precisely to the source, and using a half-silvered mirror near the source to reflect the source image to the side (Fig. 8.28). Half the light is then lost at each pass through the half-silvered mirror, and the picture brightness is reduced by  $\frac{1}{2}$ .

Conical multiple pass systems, Figure 8.29, have apparently been preferred for use in ballistic ranges because they eliminate the need for a good quality flat mirror, and are more compact. A single parabolic mirror is placed near the model flight path, and the spark source is located at twice the focal length from the mirror. If the source and its image are off axis, as shown, the double image problem occurs, but it may be minimized by flying the model near the mirror and by reducing the axis separation. The double image may be avoided by use of the half-silvered splitter mirror, with attendant light loss. Conical double-pass systems have been successfully employed to obtain laminar wake photographs at low ambient pressures (Figure 8.30 and Reference 8.8).

### 8.3.2 Theory

The basis for understanding the operation of schlieren systems has already been developed in the section on shadowgraphs. Here, we need consider only the special features of the schlieren arrangement and their effects specifically the knife edge, and the focus of the model image on the film plane.

Because of the focusing, ideally, light rays will intersect the film undeviated from positions relative to the model image they had near the model plane of symmetry. The effect of the density field thus will not be to displace the rays, but rather, to lighten or darken local exposure, through the action of the knife edge.

Refraction in the model flow field moves the image of the light source in its plane, the plane of the knife edge. Each point in the flow field is illuminated by light from all points of the source, so that though a single point  $P$  in the model's plane of symmetry, there passes a slender conical bundle of light rays, one ray from each point in the source. The point  $P$  and every point in the plane of symmetry is thus a point of virtual origin of an image of the light source. Now if all the rays passing through  $P$  are refracted through an angle  $\theta_e$ , the source image formed by these rays is displaced, since the position of this image is governed entirely by the ray directions. For a parallel light system, the image movement is  $f\theta_e$ , where  $f$  is the focal length of the image forming mirror. More generally,  $f$  may be replaced by the image distance from the mirror. Thus, instead of a single image of the source, there is an image of the source for each point in the model image.

The refracted positions of the source images, when they are toward or away from the edge of the knife, will cause the light quantity passing the edge from the points  $P$  to change. This in turn changes the brightness of the image of  $P$  on the film. This action is illustrated in Figure 8.31. If the knife edge was originally set to pass an unrefracted width,  $w$ , of the image of a rectangular source, the change in intensity of light on the film at the image of the point  $P$  may be expressed as

$$\Delta I/I = f\theta_e/w, \quad (8.25)$$

where  $\Delta I$  may be either positive or negative, depending on the direction of  $\theta_e$ . Now,  $\theta_e$  represents the total angular deflection of light rays passing through a given point in the plane of symmetry of the flow. Earlier, equations were given for the deflection  $\theta_e$  in continuously varying regions (Equation (8.20)) and at the shock waves (Equations (8.7), (8.8), and (8.9)). These deflections combine to give the total deflection  $\theta_e$ .

In schlieren photography, particular interest is directed toward the continuously varying density regions. Hence, Equation (8.20) is further developed in the following steps. First, it may be expressed in terms of the density gradient as

$$\theta_e = - \int_{z_1}^{z_f} (1 - G\rho) \frac{\partial \rho}{\partial y} dz, \quad (8.26)$$

where  $1 - G\rho \cong 1$ . Since only that component of  $\theta_e$  which is perpendicular to the knife edge is effective in changing the exposure,  $y$  in Equation (8.26) may be taken as the coordinate perpendicular to the knife edge.

For a knife edge oriented parallel to the axis of a body of revolution in axially symmetric flow, we may express  $\rho$  as a power series in the coordinate  $r$  radial to the axis, so that

$$\frac{\partial \rho}{\partial r} = a_0 + a_1 r + a_2 r^2 + a_3 r^3 + \dots \quad (8.27)$$

where the constants are functions of the axial coordinate  $x$ . They are selected, and as many terms retained as necessary, to represent accurately the density gradient profile in a given cross section of the flow. Now  $\partial \rho / \partial y$  is the component along  $y$  of  $\partial \rho / \partial r$  (Fig. 8.32) and may be written as

$$\frac{\partial \rho}{\partial y} = \frac{\partial \rho}{\partial r} \cos \phi = \frac{y}{r} \frac{\partial \rho}{\partial r} = a_0 \frac{y}{r} + a_1 y + a_2 y r + a_3 y r^2 + \dots \quad (8.28)$$

where  $r = (y^2 + z^2)^{1/2}$ . For  $G\rho \ll 1$ , the integral of Equation (8.26) may be written, with the approximation that the ray path does not deviate far from a path of constant  $y$ , as

$$-\frac{\theta_e}{2G} = \int_0^{z_s} \frac{\partial \rho}{\partial y} dz = a_0 y \int_0^{z_s} \frac{dz}{(y^2 + z^2)^{1/2}} + a_1 y \int_0^{z_s} dz + a_2 y \int_0^{z_s} (y^2 + z^2)^{1/2} dz + a_3 y \int_0^{z_s} (y^2 + z^2) dz + \dots \quad (8.29)$$

which may be integrated to give

$$-\frac{\theta_e}{2G} = \left[ a_0 y + \frac{a_2 y^3}{2} \right] \log_e \left[ \frac{z_s}{y} + \left\{ 1 + \left( \frac{z_s}{y} \right)^2 \right\}^{1/2} \right] + a_1 y z_s + \frac{a_2 y^2 z_s}{2} \left\{ 1 + \left( \frac{z_s}{y} \right)^2 \right\}^{1/2} + a_3 y^3 z_s + \frac{a_3 y^2 z_s^3}{3} + \dots \quad (8.30)$$

Thus, for a given density profile, the intensity variation over the schlieren field of view may be predicted. In principle, this can be used as a basis of comparison of theoretical density profiles with experiment.

Schlieren systems which are sensitive enough to detect continuous variations in density are normally saturated at the shock waves. Very large ray deflections can occur at the shock wave, just inside the tangent ray (see Figure 8.33, computed from Equation (8.7)). By Equation (8.25), with  $\theta_e = \delta$ , Figure 8.33 also represents relative light intensity on the film near the shock wave. When the ray deflection  $f\delta$  exceeds either the unocculted width  $w$  of the source image in one direction (Figure 8.31) or the occulted width in the other direction, saturation occurs. There is then a region of uniform illumination just inside the shock wave, either at full available brightness or at zero exposure, depending on knife edge orientation relative to the ray deflections. The saturated zone may extend well inside the shock wave location. For example, in the case represented by Figure 8.33, the deflection is 0.0033 radian at  $n/R$  of 0.2. With a 3 meter focal length mirror, this would correspond to a source image displacement of 1 cm at knife edge. The example shown is, however, more severe than many cases of interest, since  $\delta_t = 0.1$  radian corresponds to a normal shock wave with a density ratio of 5.5 at atmospheric ambient density.

If the focusing is imperfect, and in general it will be, some residual shadowgraph effect remains at the shock wave. Then the narrow dark band characteristic of the shock wave shadowgraph image is superimposed onto the schlieren effect, and quantitative interpretation becomes very complicated.

## 8.4 INTERFEROMETRY

An interferometer, as the name implies, is a device for measuring the interference between two coherent light beams, usually obtained by splitting and later recombining a single beam. In flow visualization applications, one beam, the active beam, is passed through the flow field, while the other, the reference beam, is passed around it. Unlike the other flow visualization systems discussed, the interferometer does not depend on or respond to refraction (literally, bending of the rays). Rather, it measures the retardation of waves locally (within small ray bundles) from their phase shift relative to the reference beam. Thus, the index of refraction, basically defined as the ratio of light velocity in vacuum to the velocity in the gaseous medium, is measured from the velocity itself rather than from ray deflection.

An interferometer requires exceptionally precise alignment, and also requires a monochromatic light source of very high intensity. Its optical surfaces must be very accurately ground, flat within fractions of the wavelength of light. Its supporting frame must be dimensionally stable against temperature changes and vibration isolated. As such, it is not the "rough and ready" instrument that the shadowgraph is, or even the schlieren. It is available in research only after careful design, development, and investment of time toward its perfection. Hence it is not considered a device for routine flow visualization in ballistic ranges. It is rather a special purpose instrument, quantitatively interpretable, and usually applied only to problems selected for careful study.

### 8.4.1 Optical Arrangement

The usual instrument employed in ballistic ranges (and wind tunnels) is the Mach-Zehnder interferometer. Although other optical arrangements have been used, they are in principle closely related to the Mach-Zehnder, and only the latter will be described here.

Figure 8.34 shows the basic arrangement of optics. Light from a monochromatic source is collimated to produce plane waves, of which half the intensity is reflected upward at the first half-silvered mirror to form the reference beam while the other half passes through the mirror and through the flow field to be examined. The two beams are recombined at the second half-silvered mirror where they may interfere if the instrument is well aligned. Note that half the beam energies are lost at recombination. The image forming mirror, provided where the recombined beams emerge from the instrument, is in focus on the plane of the model, so that a sharp shadow image of the model is superimposed on the interference field and refraction effects are minimized.

Although it is not the purpose of this discussion to examine in detail the practical problems of such an interferometer, it must be noted that these problems are considerable. There are problems of the light source and problems of alignment and stability of alignment. (Numerous papers have been written on these subjects - see, e.g., References 8.9 through 8.13). The light source must be of short duration to prevent model motion during exposure. If a high voltage spark is used, its output must be passed through a prism or grating monochromator or an interference filter to select a restricted wavelength region to be admitted to the interferometer. The number of fringes of good contrast depends sensitively on spectral purity of the source. Unfortunately, the bulk of the light output of the source must for this reason be discarded, leaving adequate film exposure a problem, with restrictions on both the duration and spectral band width of the light pulse. Accordingly, some investigators (see e.g., Reference 8.13) have used rotating mirror cameras to hold the image stationary on the film and permit longer durations of exposure. The laser would seem an advantageous light source for an interferometer, being by nature monochromatic and intense. At this writing, no papers describing the use of a laser light source in a Mach-Zehnder interferometer have come to the author's attention, although a novel interferometer employing holographic techniques has been reported (Ref. 8.14).

For discernible interference between the active and reference beams, their wave fronts must be nearly parallel past the recombination of the beams. Alignment of the instrument to achieve this parallelism is affected by all four flat mirrors, the two on the right affecting the active beam; the two on the left, the reference beam. Thus, once alignment has been achieved, the mirrors must be rotated in pairs to retain it. Furthermore, the mirror rotation mechanisms must be capable of very fine and slow motion, and mechanically very smooth to achieve the perfection of alignment required. The alignment is also affected by mechanical vibration and thermal expansion, so that shock mounting and the use of low expansion materials such as Invar are desirable.

To initially align the mirrors, both physical measurements for rough alignment and use of targets placed ahead of the first half-silvered mirror and viewed in the emergent beams are helpful. Alignment to equalize path lengths in the reference and active legs is needed if the source is not perfectly monochromatic, in which case the fringe contrast diminishes away from the equal-path-length fringe because of the superposition of many sets of fringes of slightly different spacing. For perfectly monochromatic light, the paths do not have to be equal, since interference need not be restricted on recombination to the same plane wave front which was split. That is, any pair of plane wave fronts can be made to interfere, depending only on their relative phase.

#### 8.4.2 Theory of Fringe Formation

If two superimposed trains of plane waves of equal wavelength are perfectly parallel, they will produce a uniform intensity on a screen or film, depending on their phase. If they are in phase, their intensities add; out of phase, their intensities subtract; and intermediate phase conditions give intermediate intensities (Figure 8.35).

If the first beam is slightly inclined to the second, the relative phase of the two families of waves varies across the field. This is shown in Figure 8.36. Constructive interference occurs at intervals, shown by the long dashed lines. Half way between the lines of constructive interference, lines of destructive interference occur. If these wave trains fall on film or a screen, the alternation of bright and dark regions is termed a series of fringes, and the distance from one bright fringe to the next is the fringe spacing,  $s$ . From the geometry, it may be seen that when the wave fronts are inclined to one another by an angle  $\epsilon$ , the fringe lines are inclined at  $\epsilon/2$  to the ray directions and

$$\frac{\lambda}{2 \cos (\epsilon/2)} = s \tan (\epsilon/2) \quad (8.31)$$

With small angle approximations appropriate to the actual values of the angle  $\epsilon$ , this may be written

$$s = \lambda/\epsilon \quad (8.32)$$

For example, with  $\lambda = 5000 \text{ \AA}$  and  $s = 0.5 \text{ cm}$ ,

$$\epsilon = \frac{5 \times 10^{-5}}{0.5} = 10^{-4} \text{ radians or } 0.0057^\circ.$$

Thus it is seen that only a minute angularity of the beams is desired (corresponding, e.g., to a rotation of a 20 cm diameter mirror by  $10^{-3} \text{ cm}$  at its edges), and that small angle approximations for  $\epsilon$  are indeed valid.

Now suppose that a local patch of one of these wave trains is delayed by having traversed a region of low light velocity. Further suppose, as an example, that this delay puts the wave system locally half a wave length behind its normal position. Locally, then, constructive interference is replaced by destructive, and vice versa

and the fringe pattern is shifted. The bright fringe becomes dark, and the dark becomes bright. Such a shift, when seen, may be interpreted as a phase shift of the wave train by  $\lambda/2$  (or more generally, by any odd integral multiple of  $\lambda/2$ ). Generalizing this observation, we may say that when the fringe shift is measured in units of the fringe space, it represents the phase shift in numbers of wavelengths. Thus

$$m = \Delta s/s, \quad (8.33)$$

where  $m$  is the number of wavelengths of retardation of the wave fronts. It will be noted that the same fringe position would occur for all values of  $m$  which differ by integers, but if the fringe shifts can be followed from a region of no disturbance to the point in question, then a value can be assigned unambiguously to  $m$ .

The fringe shift is measured from the position which the fringe would take in the undisturbed ambient gas. Since this position is not marked in an interferogram of a disturbed flow, it must be determined by interpolation of the fringe positions on either side of the disturbed flow. Now in real interferometers, fringes are not perfectly straight, nor perfectly steady. They tend to swim about a little under the influence of air motion in the room. Hence, some error in measuring fringe shift arises from lack of knowledge of the exact position of the undisturbed fringe. Since the uncertainty will usually be less than one fringe space, it is of most concern when the fringe shifts are also of this order. When fringe shifts of many fringes occur, this source of error is less important.

Immediately behind shock waves, the value of  $\Delta s/s$  is not always easy to determine, because the fringe shifts become large and the slopes are steep (see e.g., Figure 8.37). In such cases, one may either grossly reduce the ambient density (in ballistic ranges where ambient pressure may be controlled) to reduce the fringe shift and thus make it easier to trace the fringes, or use so-called white light fringes, obtained with a broader spectral band in the light source, to trace the fringes near the shock wave. With white light, only a few discernible fringes are obtained and the central fringe, because of its sharp contrast with its neighbors, can be readily traced across the flow field.

With the wave retardation determined to be  $m\lambda$  from the picture, the remaining task is to make an interpretation in terms of the flow field density distribution responsible for the retardation.

#### 8.4.3 Deduction of Flow-Field Densities

The test data to be analyzed will be either axially symmetric or three dimensional. The axially symmetric case is the easier to analyze, but in experimental practice, it is the harder to achieve, because the free-flight model in general will be at some angle of attack. Thus, for simple interpretation, a companion problem to analyzing the photograph is that of getting the photograph at small resultant angle of attack. One technique which has been used (Reference 8.15) is to place the interferometer station near an expected node in the oscillation (e.g., half a wavelength of the pitching motion from the origin of the pitch disturbance near the gun muzzle). Spheres comprise a special case. Except near the viscous wake, they will always generate an axially symmetric flow at high supersonic speeds, regardless of attitude.

Let us then describe the procedure for analysis of axially symmetric interferograms\*. We use the notation of Figure 8.32, and neglect the bending of light rays traversing the field. (This may not be permissible in all cases, but without this assumption, the analysis cannot be written explicitly. The analysis with ray deflection would necessarily be numerical, but it would proceed similarly to that given below.)

The time for a ray to traverse the flow cross section at the level  $y$  above the axis of symmetry is

$$t = 2 \int_0^{z_s} \frac{dz}{c}, \quad (8.34)$$

where  $c$  is  $c(z)$ . In the absence of flow disturbance, a wave front would advance in the time  $t$  a distance  $c_1 t$ ,  $c_1$  being the light velocity in the ambient atmosphere, whereas in the flow field, the wave front advances by  $2z_s$ . The difference is the distance by which the wave front is retarded by the presence of the flow field.

$$m\lambda = 2c_1 \int_0^{z_s} \frac{dz}{c} - 2z_s \quad (8.35)$$

The light velocity ratio,  $c_1/c$ , may be replaced by the inverse ratio of the indices of refraction,  $\zeta/\zeta_1$ , and  $\zeta$  may in turn be written as  $1 + G\rho$ , so that

$$2c_1 \int_0^{z_s} \frac{dz}{c} = \frac{2}{\zeta_1} \int_0^{z_s} (1 + G\rho) dz = \frac{2}{\zeta_1} \left[ z_s + G \int_0^{z_s} \rho dz \right] \quad (8.36)$$

\* We will assume in this discussion that ionization does not occur in the flow and that the index of refraction is determined solely by gas density. If ionization is present, the expressions for index of refraction are modified (see footnote on page 353)

Equation (8.35) thus becomes

$$m\lambda = \frac{2G}{\zeta_1} \int_0^{z_s} \rho dz - \frac{2G\rho_1 z_s}{\zeta_1}, \quad (8.37)$$

(since  $1/\zeta_1 - 1 = -G\rho_1/\zeta_1$ ). Solving for the integral, we obtain the equation relating the density distribution to the wave retardation,

$$\int_0^{z_s} \rho dz = \frac{m\lambda\zeta_1}{2G} + \rho_1 z_s. \quad (8.38)$$

Note that  $\zeta_1$  in this equation may usually be regarded as unity for practical purposes, and that  $m$  is experimentally determined from the interferogram (Equation (8.33)).

Given a density distribution, we can readily calculate  $m(y)$  and hence the fringe shift distribution by means of Equation (8.38). The reverse problem - given  $m(y)$ , calculate  $\rho(r)$  - is less convenient to solve. It is referred to in the literature as the Abel integral inversion problem. The usual approach to solution is to approximate the actual density distribution by a large number of linear segments, each linear segment corresponding to a thin annular zone. A second approach which will be described is to represent the density by a power series in  $r$  whose term coefficients are to be determined.

To perform the zone approximation solution, we first express the integral in terms of the radial coordinate  $r$  as independent variable to take advantage of the axial symmetry.

$$\int_0^{z_s} \rho dz = \int_y^{\sqrt{(y^2+z_s^2)}} \frac{\rho r dr}{\sqrt{(r^2-y^2)}}. \quad (8.39)$$

In this integral, which is performed along a light ray,  $y$  is a constant. The upper limit  $\sqrt{(y^2+z_s^2)} = r_s$ . We replace the integral with a sum of terms, one for each zone. The subscript  $i$  is used to denote the number of the inner boundary of the zone, and  $j = i + 1$  represents the number of the outer boundary. The density within the zone is represented linearly by

$$\rho = \rho_1 + \frac{\rho_j - \rho_1}{r_j - r_i} (r - r_i). \quad (8.40)$$

The contribution of the zone to the integral represented in Equation (8.38) may be obtained by inserting Equation (8.40) into the integral, it is found to be

$$\int_{r_i}^{r_j} \frac{\rho r dr}{\sqrt{(r^2-y^2)}} = A_i \rho_i - B_i \rho_j, \quad (8.41)$$

where

$$A_i = r_j \frac{\sqrt{(r_j^2-y^2)} - \sqrt{(r_i^2-y^2)}}{r_j - r_i} - \frac{y^2}{2(r_j - r_i)} \log_e \frac{r_j + \sqrt{(r_j^2-y^2)}}{r_i + \sqrt{(r_i^2-y^2)}},$$

and

$$B_i = r_i \frac{\sqrt{(r_j^2-y^2)} - \sqrt{(r_i^2-y^2)}}{r_j - r_i} - \frac{y^2}{2(r_j - r_i)} \log_e \frac{r_j + \sqrt{(r_j^2-y^2)}}{r_i + \sqrt{(r_i^2-y^2)}} \quad (8.42)$$

Note that  $y$  is determined by the location of the ray being analyzed, and  $r_i$  and  $r_j$  are known numbers for each zone. Hence, the coefficients  $A_i$  and  $B_i$  are known. The total integral along the ray is the sum of terms similar to Equation (8.41) for each of the zones traversed and may be written

$$\int_0^{z_s} \rho dz = \int_y^{r_s} \frac{\rho r dr}{\sqrt{(r^2-y^2)}} = \sum_{i=1}^N (A_i \rho_i - B_i \rho_j). \quad (8.43)$$

Here,  $i = 1$  at  $r = y$ , and  $N$  is the total number of zones between  $y$  and  $r_s$ . The value of the integral is obtained from the interferogram through Equation (8.38). Hence, the gas density at one zone boundary may be unknown in Equation (8.43) and be determined from it. This boundary is tangent to the position  $y$  of the ray being analyzed. The densities at all zone boundaries outboard of this will have been determined in sequence, progressing from the shock wave inward.

For the calculation to start, the density immediately behind the shock wave must be determined. If the flow field is known to be in chemical and thermodynamic equilibrium, this can be done most simply from a measurement of the shock wave inclination and reference to shock wave tables. If  $\rho_s$  is to be determined from the experiment, it is necessary to make a one zone calculation at the shock wave and to assume that  $\rho = \rho_s = \text{constant}$  within the zone.

This leads to

$$\int_0^{z_s} \rho \, dz = \rho_s \int_y^{r_s} \frac{r \, dr}{\sqrt{(r_s^2 - y^2)}} = \rho_s \sqrt{(r_s^2 - y^2)} = \frac{m y \lambda \zeta_1}{2G} + \rho_1 z_s \quad (8.44)$$

from which  $\rho_s$  may be obtained. The zone for this determination,  $r_s - y$ , is chosen thin to minimize the variation of density within the zone. The density determined is more properly plotted at the center of the zone than immediately behind the shock wave.

Tables of coefficients for these calculations, corresponding to (but not identical to)  $A_1$  and  $B_1$ , have been published in Reference 8.16 for a 50 zone division of the flow field. The use of these tables can make the reduction less laborious. Of course, with modern electronic computers, the labor of this analysis is of less concern than it was formerly.

The series representation method - the second method noted earlier - is computationally simpler but may present difficulties in cases where the density profile is not smooth. It is analogous to the approach used earlier to obtain expressions for flow deflection angles for schlieren and shadowgraph applications, Equations (8.27) through (8.30). Here, however, we represent the density rather than the density gradient by the power series,

$$\rho = \rho_0 + a_1 r + a_2 r^2 + a_3 r^3 + a_4 r^4 + \dots a_{n-1} r^{n-1} \quad (8.45)$$

Note that in this expression,  $\rho_0$  is the density on the axis of the flow, where  $r = 0$ , and is fictitious for stations of the flow where the body occupies the axis. Now, since we wish to evaluate  $\int_0^{z_s} \rho \, dz$ , we put Equation (8.45) in terms of  $z$ ,

$$\rho = \rho_0 + a_1 \sqrt{(y^2 + z^2)} + a_2 (y^2 + z^2) + a_3 (y^2 + z^2)^{3/2} + a_4 (y^2 + z^2)^2 + \dots \quad (8.46)$$

This expression may be substituted into the integral and evaluated term by term to obtain

$$\begin{aligned} \int_0^{z_s} \rho \, dz = & \rho_0 z_s + \frac{a_1}{2} \left[ z_s r_s + y^2 \log_e \frac{z_s + r_s}{y} \right] + a_2 \left[ y^2 z_s + \frac{z_s^3}{3} \right] + \\ & + \frac{a_3}{4} \left[ z_s r_s^3 + \frac{3}{2} y^2 z_s r_s + \frac{3}{2} y^4 \log_e \left( \frac{z_s + r_s}{y} \right) \right] + a_4 \left[ y^4 z_s + \frac{2}{3} y^2 z_s^3 + \frac{z_s^5}{5} \right] + \dots \quad (8.47) \end{aligned}$$

Now for any given axial station of the flow,  $r_s$  may be measured from the interferogram,  $y$  is selected by the analyst, and  $z_s = \sqrt{(r_s^2 - y^2)}$ . Hence, the bracketed multipliers of the coefficients  $a_1, a_2, a_3, a_4, \dots$  in Equation (8.47) are known numbers. By choosing a number of values of  $y$  for analysis at a given axial station of the flow, we may write Equation (8.47) as many times as we please, with values of the bracketed multipliers appropriate to each value of  $y$  chosen. If we write in this way the same number of equations as terms used to define  $\rho$ , we may solve these questions simultaneously to define  $\rho_0, a_1, a_2$ , etc., and hence obtain a representation of the density profile across the flow field at that station. If we write more simultaneous equations than the number of unknowns, then least squares methods may be used to obtain a best fit.

Although five terms have been retained in representing the density profile above, more or fewer terms can be retained. Sometimes, higher order terms in a series will improve the fit to a few measured points, but introduce physically unrealistic inflections in the curve. When the number of measured points is large, or the data are faired continuously, more terms in the series should be of advantage. This is a matter for study in individual applications. The picture of a slender cone shown in Figure 8.38 has been analyzed by the power series method to obtain the results shown in Figure 8.39 for one and two term approximations. The one term approximation, where density is regarded as constant along each light ray, but variable from ray to ray, already shows the character of the distribution and may be hand calculated very quickly. The one-term densities have been plotted both at  $y$  (the location at which fringe shift is measured) and at  $(y + r_s)/2$  to bracket the position at which they would be expected actually to occur, and these two curves do indeed bracket the two term approximation. The two term approximation requires data at only two values of  $y$  to define a series of values of  $\rho_0$  and  $a_1$ , hence was solved locally between every adjacent pair of fringe-shift measurements, of which there were 4 in all, corresponding to the fringes intersected by a plane normal to the model at the station analyzed. The locally derived segments, which are entirely independent, come very near to intersecting and forming a continuous curve. A fairing of these two term solutions is shown by the long dashed curve. The agreement of the two-term solutions and their fairing with conical flow theory is reasonable considering that the model was at an angle of attack at  $1.25^\circ$  and that it was the windward side which was analysed. Note that the sensitivity of the interferometer has permitted definition of detail even though the density is only a few percent above ambient.

#### 8.4.4 Reported Applications

Because of the difficulty of the method, both experimentally and analytically, there have been comparatively few applications of interferometry to obtain quantitative density distributions around projectiles in ballistic ranges. There have been several applications to spheres, because the symmetry requirement is satisfied and

because of fundamental interest in flow about spheres. A beautiful interferogram of a 90 mm sphere tested at the Ballistic Research Laboratories at a Mach number of 5.7 and a range pressure of 0.05 atmospheres is shown in Figure 8.40. Results of analyses of the flow field of a sphere have been presented and discussed in References 8.17 and 8.18. It is difficult to achieve accurate spatial resolution in the forward part of the shock layer because it is thin (see especially Figure 8.37). On the other hand, density is slowly changing in this region, so that a high degree of spatial resolution may not be required, except for purposes of detailed comparisons with theory.

Cone flow fields also have been analyzed (Reference 8.19). When cones are slender, their fringe patterns are slowly varying and permit accurate measurement (Figure 8.38). When the cone angle is large, problems are analogous to those of other low fineness ratio bodies. Low ambient densities favor clear identification of fringe shifts, but may introduce non-equilibrium flow effects. These were the subject of study in Reference 8.20 which, while it was a study in an expansion tube, could equally have been performed in a ballistic range. Cones may be used to test the validity and accuracy of the analysis procedure and the instrument, since a wide range of theoretical solutions is available.

Interferometry has also been used to investigate density profiles in turbulent boundary layers on models in a ballistic range (Reference 8.15). Long conical and ogive-cylinder models were selected to maximize the boundary layer thickness, and precautions were taken to minimize the angle of attack at the interferometer station. Figure 8.38 is an interferogram from this investigation, and Figure 8.41 shows an enlargement of fringes in the boundary layer. The boundary layer fringe shifts are appreciable and indicate the presence of density variations associated with turbulence. The boundary layer fringes were analyzed assuming axial symmetry (which, because of the fluctuations, does not precisely obtain), and both the mean density profiles and the fluctuation levels were determined. It was also possible, with the aid of an energy balance, to deduce the heat transfer rate to the model from the measurements.

## 8.5 RESEARCH APPLICATION OF SHADOWGRAPH AND SCHLIEREN PICTURES

Now let us review some of the ways shadowgraph and schlieren photographs have been used in research in ballistic ranges, and thereby indicate how they may be used, in a general sense. The discussion which follows is organized under eight topics - Shock Wave Location and Shape, Boundary Layer Transition and Turbulence, Separated Flow, Base Flow Configuration and Base Pressure, Wakes, Determinations of Local Mach Number and Static Pressure, Density Ratios and Non-Equilibrium Flow, and Additional Phenomena (outside the other categories). A logical place to begin is with the most prominent features of supersonic flow fields, the shock waves.

### 8.5.1 Shock-Wave Location and Shape

From what has already been said, it is clear that the shock wave may be located in a shadowgraph or schlieren picture from the position of the last undisturbed light ray upstream of the wave, i.e., the ray tangent to the shock wave envelope. Measurements of the coordinates of a series of points along the bow shock wave require correction only for any magnification that may be present (or, in parallel light systems deviations of rays from perfect parallelism). Measurements of this kind have been used to test theoretical calculations of shock wave shape, and as inputs to the computation of downstream flow fields<sup>8,21</sup>. It has been found from such measurements that bow shock waves can often be well represented by power law expressions of the form  $y = kx^m$ , or by connection of a series of such expressions<sup>8,22</sup>.

A second important property of bow shock waves is the stand off distance from blunt bodies, or the analogous property for cones, the stand off angle. This distance or angle may be directly measured from the above-noted criterion for location of the shock surface, but may be significantly in error if refraction in the shock layer distorts the location of the body surface. This error is minimized by (a) focusing the shadowgraph on the plane of flight, and (b) operating at low air densities. It may also be corrected by theoretical analysis of the emergent angle of the light ray tangent to the body surface. Particularly obvious errors will occur when the dark and light bands produced at the wave extend across the shock layer and overlap the model (Figure 8.6(c)). No useful measurement can be expected in such a case. For highest accuracy, correction for diffraction at the shock and model surfaces may be required. To illustrate that a useful degree of accuracy can be obtained without the latter corrections, but with the restriction of shadowgraph sensitivity and air density to give favorable conditions for such measurements, Figure 8.42 is reproduced from Reference 8.23.

In addition to bow shock waves, secondary or embedded shock waves are of significant interest. An example is the shock wave generated on a flared afterbody (Figure 8.43) or other stabilizing or control surface. From the standpoint of configuration aerodynamics, it is important to know the flow configuration, since the forces and stability are sensitive to the shock waves present. Since the light rays recording embedded waves traverse the bow shock wave and intervening density field, distortions of positions can be expected. The locations of embedded shock waves relative to adjoining body surfaces, however, should be recorded fairly accurately, since the distortions to the absolute location of the shock surface and body surface due to the surrounding flow field are similar.

Interest may also be directed to the interference of shock waves with downstream body surfaces. For example, when a bow shock wave impinges on or passes near the location of a body surface, the bow wave may be deflected (strengthened), as in Figure 8.44. Actually, in this case there is an intersection of the bow wave with an embedded shock wave, and reflection of the embedded wave off the bow wave may be observed. Also, emerging from the intersection, a discontinuity streamline appears and undergoes transition to turbulence. The embedded wave

is not formed on the leeward surface of the flare. In this example, the wave interaction occurs because of angle of attack, but on appropriate configurations, it may occur at the equilibrium flight attitude. Flow photographs document the occurrence and give details of the resulting flow configuration.

Figures 8.43 and 8.44 were obtained as part of the investigation reported in Reference 8.24.

### 8.5.2 Boundary-Layer Transition and Turbulence

A very rich and interesting use of shadowgraphs has been the observation and investigation of boundary layer transition phenomena. Under favorable conditions, this method of detecting transition is of great value, giving information not available from methods traditionally applied in wind tunnels. The optical method, developed in ballistic ranges, has therefore found application in wind tunnels also.

The visibility of turbulence in shadowgraphs, e.g., Figures 8.13 and 8.16, implies that the place where turbulence begins, the laminar-turbulent transition location, should be observable. However, since the turbulent boundary layer may be initially very thin, the question arises as to whether it can be detected in its early stages - i.e., the eddies might be initially too small to observe within the limits of diffraction at the model edge, film grain, etc.

Experience has shown<sup>8.25, 8.26</sup> that thin turbulent boundary layer conditions can occur under which discrete eddies cannot be individually identified. Under these conditions, however, the eddies collectively still give characteristic appearance to the boundary layer, and in addition may give indirect evidence of their presence by generating a field of sound waves which can be seen in the adjoining flow (see, e.g., Figure 8.45). Note in this figure that the noise field is bounded by a Mach wave at an inclination appropriate to the boundary layer edge Mach number. Tracing this wave to its point of origin identifies the forward limit of the boundary layer region which is generating a noise field. It may be assumed that this point is the instantaneous point of boundary layer transition.

The transition point obtained from such an observation may be compared with that given directly by the appearance of the thin turbulent boundary layer. In regions where discrete eddies cannot be resolved, models with thin turbulent boundary layers have been described as having a "hairy" appearance along their edges<sup>8.25</sup> (Figure 8.46). When the eddies are small, the density gradients are very large, and light may be refracted to much greater distances than the eddy diameter. Thus, in Figure 8.46, we see shadow filaments projecting well outside the boundary layer along the model's forward surfaces, beginning near the tip. A glance at the model base region leaves no doubt that the boundary layer is turbulent as it comes off the base. A sound field from the boundary layer can also be seen within the shock layer. If the limits of the hairy region coincide with the limits of the noise generating region, confirmation of two independent techniques for locating transition has been obtained.

A further test can be applied to the selected location of boundary layer transition on long models which attain appreciable boundary layer thickness. From selected individual photographs, one can measure the boundary layer thickness and plot it against streamwise distance on logarithmic paper to obtain, ideally for conical and cylindrical models, a straight line growth curve (see Reference 8.15 for plots of this kind). Extrapolation forward to the point where the theoretical laminar boundary layer thickness is matched will yield a transition point estimate which can be compared with the other two determinations.

It was implied above that the instantaneous location of transition to turbulence is time dependent. This is indeed the case. Views of the same model meridian in successive photographic stations generally show different locations of transition, and may also show the presence of short duration bursts of turbulence (Figure 8.47). These may proceed separately along the surface, precede a steadier turbulent boundary layer, or be superimposed on other bursts or on the steadier turbulent boundary layer. The mean location of transition may furthermore differ on different meridians, because of the presence of microscopic roughness elements along those meridians. Angle of attack also, for slender bodies, has a first order, determining influence on transition. Thus, no single picture can be taken as definitive of the boundary layer transition on a given model flight. Rather, the effects of unsteadiness, meridional differences (due to surface roughness or tip asymmetry), and angle of attack must be carefully isolated in a series of pictures, normally requiring a series of test firings. The unsteadiness by itself leads to a region of intermittently laminar and turbulent boundary layer which has been identified, from ballistic range studies and from hot wire anemometer studies in wind tunnels, as the transitional boundary layer zone defined by other, time-averaging techniques of observing transition (see, e.g. Reference 8.26).

The fact that the noise-field-bounding Mach line may have a slope appropriate to the boundary layer edge Mach number indicates that the transition point generating this field is at least momentarily stationary, or moving slowly on the surface. In the case of bursts, however, the shock wave attached to their leading edges is seen to be much steeper than the stationary disturbance Mach angle, because bursts are in rapid movement backward along the surface. The slope of the wave may be used to determine the speed of movement of the upstream edge of the burst down the surface, which is found to be about 6/10 of the boundary layer edge velocity. It has also been found possible to define the shapes of bursts in profile and plan view from their shadowgraph images<sup>8.27</sup>. The profiles were obtained by careful thickness distribution measurements, while the plan dimensions were deduced from bursts wide enough to appear on two or more of the four visible meridians in simultaneous orthogonal shadowgraphs. Correlation of the measurements of a large number of bursts was necessary in order to arrive at a representative definition of shape. The shapes obtained by this technique were found to relate closely to shapes previously determined by other techniques in wind tunnels. The growth patterns of bursts were also deduced by relating size to distance from the model leading edge or from the observed disturbance point responsible for the bursts.



The measurement of turbulent boundary layer thickness from shadowgraphs is seemingly straightforward, except for difficulties posed by the irregularities of its outer edge, but it is also subject to certain optical inaccuracies. The edge irregularities, illustrated in the preceding figures, are an inherent feature of the turbulent boundary layer. The thickness at a given point and at a given instant is sharply defined, but like the transition point, the thickness at any station varies with time, and can be fully described only statistically. The simplest statistical approach is to measure the actual thickness at a large number of positions along the surface, plot these measurements, and let the eye fair a mean line. Whether a more formal approach is justified will depend on the quantity and quality of the data available.

Distortions of the boundary layer thickness recorded on film have been discussed earlier. They may arise from three sources: (a) eddy refraction, causing the eddy images to be larger or smaller than their actual diameters. (b) refraction in the steep density gradient of the inner part of the boundary layer, causing the model edge to be displaced. (c) refraction through the surrounding flow field, causing a (nearly equal) displacement of the boundary layer edge and the model edge. Of these three contributions, the third seems to be of least concern, being nearly self compensating. The second can be of major concern, as noted earlier. The first source of distortion, due to eddy refraction, can only be evaluated theoretically, or by comparison of boundary layer thickness measurements obtained with those given by a different measuring technique. Such comparisons are necessary if the measurements are to be regarded as more than a rough indication of the boundary layer thickness.

Additional features of the structure of the steady state turbulent boundary layer may be observed in shadowgraph pictures. The correspondence between the theoretical image of an eddy and the spot patterns seen in turbulent boundary layers has been noted in an earlier section. Close study of these patterns reveals that the spot images are nearly of uniform diameter for a wide variety of test conditions, and that they are arrayed in single file order during early stages of boundary layer growth (to Reynolds numbers of  $10^7$ ) (Reference 8.15). When the boundary layer thickness begins to exceed the diameter of a single spot, the spots are found in staggered rows, two deep. This process develops until as many as five spots are seen across the thickness of the boundary layer. At this stage, one can find repeated patterns where the spots are arrayed in slanted lines, inclined to the surface at about  $45^\circ$  (Reference 8.15). These configurations are thought to be related to "horseshoe vortices" reported from studies of low speed boundary layers by other visualization techniques, and which are also inclined to the surface in this way.

The use of flow visualization for transition and turbulent boundary layer studies is, of course, limited to favorable optical and fluid dynamic conditions. First of all, the Reynolds numbers must be large enough to generate turbulent flow (greater than about  $10^6$ ). In addition, the model to be studied must be large enough to develop appreciable boundary layer thickness (which is roughly proportional to the 0.8 power of the length of run along the model), since observation of thin boundary layers is difficult and may not be definitive. Third, shock waves should not lie so close to the body surface as to obscure a clear view of the boundary layer (studies of slender pointed bodies at very high speeds encounter difficulty in this respect). Fourth, the gas densities must be high enough to produce appreciable eddy refraction (note that this requirement is usually satisfied if the first requirement is satisfied). At low subsonic speeds, shadowgraph visualization of turbulence tends to be lost because the density gradients are small in low speed flow. Thus, the technique is not universally available. However, when it can be applied, it is a very powerful and informative one.

### 8.5.3 Separated Flow

Flow separation on ballistic range models is often associated with stabilizers, such as conical flares, forward facing steps (e.g., Figure 8.18), or backward facing steps, of which the blunt base is an almost universally present example. The photographic indications of flow separation are: (a) the boundary layer image may be seen to leave the surface. (b) An oblique shock wave may be formed by the turning of the external flow at the separation point. (c) Reattachment phenomena, such as additional shock waves or gathering compressions, may be seen at a reattachment point.

The details seen differ, depending on whether the boundary layer approaching the separation point is laminar (Figure 8.48) or turbulent (Figure 8.49). When it is turbulent, the separated region is conspicuously filled with turbulent eddies. When it is laminar, the shadowgraph image of the separated boundary layer appears as a smooth line bounding the separated region. Such a line is clearly visible on the bottom side of the model in Figure 8.48, extending from a separation point ahead of the midlength station of the model to a reattachment point near the center of the flare. The separation shock wave is weak but discernible, while the reattachment shock wave is stronger, and replaces the embedded wave which would, in the absence of separation, originate at the flare-cylinder intersection. (The background of turbulence in this picture comes from the boundary layer on the windows of the Supersonic Free-Flight Wind Tunnel, a counterflow facility where the photograph was obtained).

Another type of separation results from the inability of a flow to negotiate a convex corner; this type of separation is frequently seen at the sharp or slightly rounded corners of the face of blunt bodies. This is illustrated clearly at the outermost corner of the step in Figure 8.18. The thick turbulent region behind the corner clearly indicates separation. Separations of this kind are often, unlike Figure 8.18, very local, with reattachment occurring immediately behind the corner, accompanied by a reattachment shock wave. Laminar separated regions of this kind are sometimes so thin that their presence can be definitely determined only from the presence of the reattachment shock wave. Figure 8.10 shows a very strong reattachment shock wave in a case where the separated streamline can be clearly seen.

#### 8.5.4 Base-Flow Configuration and Base Pressure

Shadowgraph pictures contain a wealth of descriptive information on the configuration of base flows (see, e.g., Figures 8.16, 8.17, and 8.19). When a model terminates in a bluff base, the flow must expand to reoccupy the full cross section behind it. This process begins in a Prandtl-Meyer expansion fan at the base corner. As noted earlier, in the section on images of flow features, and as may be seen in these pictures, the first and last Mach line of the expansion fan are made visible by the shadowgraph. The flow is turned toward the axis by the expansion, and the laminar (Figure 8.16) or turbulent (Figures 8.17 and 8.19) boundary layer coming off the model becomes the boundary of the dead air (separated flow) region behind the base, and leaves its image in the picture. If transition occurs along this boundary, that may be seen (Figure 8.16). The inward directed flow must be turned parallel to the main flow direction again, and this is accomplished in a compression region - usually not a single, discrete oblique shock wave. The multiple shock waves of the compression soon coalesce into a single shock wave, however. The boundary layer passes through a minimum section, usually termed the neck of the wake, near the region of origin of this closing shock wave. Beyond the minimum section, the boundary layer air and air subsequently entrained by it comprise the viscous wake.

Besides the conspicuous differences between laminar and turbulent base regions due to the visibility of turbulence, systematic differences in flow geometry also are found. Since turbulent boundary layers involve more mass flow, they tend to have a larger diameter wake neck at a given Reynolds number, and furthermore, the distance downstream from the base to the minimum section is different (Figure 8.50). (These two pictures were obtained at nominally equal test conditions. Differences in the boundary layer and wake were a result of microscopic differences in roughness and symmetry of the model tip. The different flow configuration is accompanied by a difference in base pressure).

The downstream distance to the neck is sensitive also to Reynolds number, particularly with laminar flow. At very low Reynolds numbers, the wake may actually be initially divergent. The angle of convergence of the wake is, in addition, Mach number dependent, becoming smaller at low Mach numbers, and slightly divergent under some subsonic flow conditions. This tendency for initial divergence at low supersonic Mach numbers is illustrated by Figure 8.18.

Although a low speed recirculating flow exists in the dead air region (and in separated flows generally), no evidence of this is provided in the shadowgraphs. An interesting phenomenon which is made visible is the formation of streamwise vortices in the separated laminar boundary layer, as an intermediate stage of transition to turbulence. Attention has already been called to these vortices, marked by dark cores bounded by light edges, in the base region of Figure 8.16. They can also be seen in the upper picture of Figure 8.50.

We can fully explain the lines bounding the Prandtl-Meyer expansion fans on the basis of earlier sections on particular flow features and diffraction effects. For example, the final Mach line of the fan is located along the inner boundary of the dark (unexposed) band (Figure 8.12). Diffraction may contribute a light fringe along this boundary of the band, to give it the appearance of a shock wave. It is believed that this pattern has in some cases led to discussion of a "lip shock wave" in the literature. It is, however, possible for a weak shock wave to form along an initially curved edge of the separated flow region, and shock waves may, in some instances, occur there.

The base pressure can be estimated from the image of the flow configuration by two independent methods. The first is based on a measurement of the angle through which the streamlines turn in coming off the model base to the direction of the boundary layer image behind the base<sup>8,28</sup>. This method has been applied in the example of the preceding Chapter. The boundary layer line image is considered the boundary for an inviscid Prandtl-Meyer expansion. (This may be in error to the extent that the boundary layer affects the expansion). The pressure and Mach number preceding the expansion are required, but for cones, e.g., these are readily available from theory. The measured turning angle may be used to enter tables of Prandtl-Meyer flow (e.g., for perfect air, Reference 8.29), to determine the pressure after expansion - the boundary pressure of the base region\*. Since flow velocities in the dead air region are small, it is presumed that no large pressure difference can exist within it.

The second method requires measurement of the Mach angle after expansion, the angle between the final Mach line of the expansion and the streamline direction as given by the boundary layer image. From the Mach angle  $\beta$ , the local Mach number  $M$  may be calculated ( $\sin \beta = 1/M$ ). The ratio of local (base edge) static pressure to total pressure  $p/p_t$  is a function of the Mach number, available in tables for both perfect and real gases. Since the flow may be assumed isentropic except at the shock waves, the total pressure is calculable (for streamlines near the body surface) from the flow tables and shock wave tables, given the shock wave slope at the model apex. Hence, the base edge pressure may be computed. An advantage of this method is that it does not require knowledge of pressure and Mach number on streamlines approaching the model base, and hence may be applied in cases where theoretical solutions for the forebody flow field are not available.

#### 8.5.5 Wakes

The visibility of turbulent wakes has been evident in many of the pictures discussed thus far. These pictures invariably show turbulent spot patterns, the spots being of remarkably uniform size. The grouping of the spot patterns into turbulent clusters gives irregularity to the edge of the wake, which, in many pictures, is strongly suggestive of a helical or "corkscrew" pattern.

\* Although the expansion becomes three dimensional some distance away from the corner, it may be considered two-dimensional at radial distances from the corner small compared to the body base radius. To make the use of two-dimensional tables valid, then, it is necessary to measure the angles as close to their initial values as practicable. It is also emphasized that optical distortion of these angles can be present, as can flow distortion by the boundary layer.

Laminar wakes downstream of the trailing shock wave have not been seen as often in routine ballistic range testing because at the Reynolds numbers associated with fractional atmosphere ambient pressure, the boundary layer is seldom stable enough to run along the separated flow region and pass through the trailing shock wave system and remain laminar.

Interest in wakes very far downstream has been stimulated by observations of entry vehicles coming into the atmosphere, which may leave ionized trails thousands of feet long. A number of techniques have been applied in ballistic ranges for measuring the properties of these wakes. (Some are described in Chapters 10 and 11). Two areas of interest have been served by studies employing optical examination of wakes in shadowgraph and schlieren pictures. These are the Reynolds number of laminar-turbulent transition in the wake (at very low body length Reynolds numbers); and the rate of growth of wakes in the far downstream region.

For the study of these problems, the firing of the light source may be delayed until the model has traveled a desired distance (as much as  $10^2$  to  $10^4$  diameters) past the photographic station. Alternatively, the last station in the range may be used to trigger all the stations simultaneously to record the instantaneous configuration at a series of positions along the wake<sup>8.30</sup>. The turbulent wake "diameters" measured from shadowgraphs are, of course, irregular and must be interpreted statistically.

The laminar wakes produced at very low range pressures (order of 0.01 atmosphere) are visible only in highly sensitive optical systems. Double pass schlieren systems have been used to make these flows visible. Figure 8.30 is one such picture, obtained with the knife edge horizontal, at a body length Reynolds number of about 60,000. First indications of transition appear about 10 diameters downstream of the base of the  $12\frac{1}{2}^\circ$  half-angle cone. Although the base flow pattern is not strongly convergent, a trailing shock wave originates near the wake neck about 2 diameters behind the base. The rate of growth of the wake is seen to be slow within the region covered, and it appears that approximate measurements of the rate of growth of the laminar wake could be obtained from pictures of this kind. The experimental conditions of this photograph are further discussed in Reference 8.31.

#### 8.5.6 Determination of Local Mach Number and Static Pressure

Wherever Mach wavelets are generated by body-fixed disturbances and recorded in flow pictures, e.g., Figure 8.51, especially on the upper surface of the sphere, it is possible to determine both the local Mach number and static pressure near the body surface. The local Mach number is determined from the angle  $\beta$  between the Mach wave and the local streamline direction, which at the surface is tangent to the body, by the well known relationship between Mach number and Mach angle,  $M = 1/\sin \beta$ . The static pressure may be calculated from the local Mach number with the assumption that the flow is isentropic except in passing through shock waves. (The effect of the shock waves on flow total pressure is calculable from shock wave theory, see, e.g., Reference 8.32, from the slopes of shock waves traversed by streamlines near the body surface).

To generate such Mach wavelets, shallow grooves may be machined on the body at selected locations. To avoid undue disturbance to the flow, they should be of the minimum depth needed to generate a visible wave. From a properly distributed set of these grooves, surface pressure distributions may be derived.

The Mach waves may remain visible well away from the surface where, in general, they become curved. If the stream direction and points of streamline crossing of the shock waves are known for off-surface locations, local Mach number and static pressure are, again, defined. A few streamlines may be marked by intersection with the bow wave of shock waves generated by accidental or purposely located disturbance generators near the model nose. The combination of marked streamlines and Mach waves would make it possible to obtain a considerable definition of the flow field surrounding a body, particularly a slender body at moderate supersonic Mach number.

In the past, these techniques have been used only occasionally to determine base pressures and surface Mach numbers at isolated points. They would seem to be capable of much more, in principle providing a way of obtaining from ballistic ranges information normally conceded to be outside their measurement capabilities.

#### 8.5.7 Density Ratios and Non-Equilibrium Flow

Three techniques have been identified for determining indirectly the density ratios across bow shock waves. Two of these have been applied<sup>8.33, 8.34</sup>. Through comparison of the density ratios determined with equilibrium values given by theory, the presence of non-equilibrium flow can be investigated. One technique, limited to conical flow fields, is capable of giving relaxation times for non-equilibrium processes.

A technique applicable to blunt nose bodies, originally described in Reference 8.33, is based on the dependence of bow shock wave stand off distance on the density ratio at the shock wave in the stagnation region. (For spherical noses, the relation  $\delta/R = 0.78(\rho_1/\rho_2)$  has been established as accurate within a few percent<sup>8.23, 8.35</sup>. Here,  $R$  is the body nose radius of curvature and  $\rho_1/\rho_2$  the ratio of ambient to shock layer density in the stagnation region). Measurement of the stand-off distance of spherical-nosed bodies may thus be interpreted to define stagnation region gas density. Comparison of densities determined with those tabulated theoretically for chemical and thermodynamic equilibrium behind the shock wave (e.g., Reference 8.36) will indicate whether equilibrium is attained in the experiment. Calculations can also be made of density ratios with some of the degrees of freedom equilibrated to provide further interpretation of what is observed.

A related technique, applicable to shock waves on cones, can be used to determine relaxation times<sup>8.34, 8.20</sup>. In this case, it is the angular separation of the bow shock wave from the model face - the stand-off angle - which depends on the density ratio. The initial wave angle at the tip is determined by the unrelaxed gas and is therefore larger than the equilibrium angle. At large enough distances from the apex for the bulk of the flow in the shock layer to have equilibrated, the wave slope becomes asymptotic to the equilibrium slope. At low ambient pressures, equilibration may never occur within the physical length of the model, while at high ambient pressures, the non-equilibrium zone may be very local, confined to the region of the tip, and may not be observable. The intermediate regime, where shock wave curvature may be visible and measurable, leads through theoretical interpretation to the relaxation time<sup>8.34</sup>.

Still another technique for determining density ratio is the measurement of the dark band width of the shock wave in shadowgraphs, discussed in an earlier section. This is directly an optical technique, since the index of refraction in the shock-compressed gas is the property determined, and is directly related to gas density (for velocities at which ionization may be neglected). When ionization becomes the dominant process affecting the index of refraction, experimental studies of the degree of ionization immediately behind the wave could conceivably be approached on this same basis.

#### 8.5.8 Additional Phenomena Sometimes Seen in Shadowgraphs

There are many interesting and informative phenomena seen occasionally in shadowgraph pictures which do not fall under the above headings. We will mention and show examples of some. These include evidences of high frequency oscillations in otherwise steady flows; unusual configurations in base flows; evidences of model damage, deformation, burning in flight, or surface spalling; and evidences of soot particle condensation from products of ablation of organic model materials.

High frequency oscillations have been recorded emanating from shallow spanwise or circumferential V-grooves, machined near model leading edges to act as boundary layer trips. An example occurs near the wing leading edge of the airplane model in Figure 8.52. There were several grooves a few thousandths of an inch deep machined parallel to and near the wing leading edge. The oscillation indicated by the train of waves coming from this vicinity, at a frequency of the order of 250 kilocycles/second, is believed to result from correlated pulsating flow into and out of the grooves. (The trip was effective in starting turbulence at a chord Reynolds number less than  $10^6$ ).

Unsteady waves have also been recorded in the stagnation region of blunt body shock layers<sup>8.37, 8.38</sup>, in the absence of grooves or other intentionally placed roughness. These waves (e.g., Figure 8.53) are less regular than the waves of Figure 8.52, and their origin is uncertain. They are not always seen in such flows. One possible cause is unsteadiness of boundary layer transition. Another is minute grooves left on the surface in machining and polishing. It is not difficult to imagine oscillations rebounding across the thickness of the shock layer, compressions reflecting as compressions off the solid surface and as expansions off the shock surface, once a source of initial disturbance has been introduced<sup>8.39</sup>.

An example of a very regular boundary layer transition process in the base flow of a blunt body is shown in Figure 8.54. Transition occurs at a nearly constant station around the wake periphery, and evidences of vortices transverse to the flow are presented by line images spanning parts of the base region. The profile views of these vortices, seen at the outer boundaries of this station of the wake, appear as small black cores. Pictures presented in this chapter have shown the diversity of processes by which laminar boundary layers become turbulent.

Experimenters will always inspect their shadow pictures closely for model damage, which may range from catastrophic to minute. Supersonic flow over a surface helps provide evidence of minor damage, such as upset joints, by generating Mach waves where the surface is not smooth and continuous. Note that the model in Figure 8.17 shows joint imperfections both at a forward station on the cylinder and at a station near the base of the flare, both of which are so small as to be almost imperceptible in the model shadow image. Figure 8.55, while not of very general significance, presents the intriguing picture of a model being pulled apart in flight by the drag force on the flare. The friction available on the nose plug was not sufficient to provide the incremental force needed to give the heavy nose the same deceleration as the drag force gave to the complete model.

Three kinds of model surface reaction to its thermodynamic environment are recorded in Figures 8.56 through 8.59. The model in Figure 8.56 had a titanium nose which was ignited in flight by aerodynamic heating and it burned chemically as it flew. The image of the flame was recorded as a bright streak exposure in the focused shadowgraph. Other models in this series were flown at the same conditions without igniting. The phenomenon in Figure 8.57 has been seen many times when heating rates become very large (greater than  $10^4$  watts/cm<sup>2</sup>). Surface spalling is apparently induced in some materials at these rates, and small particles are explosively ejected from the surface to fly momentarily as small companions to the test model. The spalling has been observed to be continuous throughout the flight and surface erosion is clearly evident in later pictures. More intense spalling or material ejection is represented in the photograph of Figure 8.58. Here, the ejections are so large and frequent that the contour of the shock wave is affected over the entire field of view. Gas evolution may be the principle phenomenon here, since no clear evidence of large solid particles appears. Figure 8.59, shows a dark shadowed wake and is typically obtained when carbon-rich organic materials, such as polycarbonates (trade names - Lexan, Zelux), are used for models<sup>8.40</sup>. This wake is brightly luminous when scanned with radiometer instrumentation such as is described in Chapter 9, and has a grey body spectrum, at a temperature of about 4000°F, with molecular bands superimposed. The partial opacity in the shadowgraph, the grey body spectrum, and the high atom ratio of carbon in the material have indicated that carbon condensation occurs to form minute soot particles in the ablation products in the wake<sup>8.40</sup>.

The above discussion is not comprehensive, but it suggests the nature of the many interesting, miscellaneous phenomena which occasionally appear in high speed flow pictures.

#### 8.5.9 Correlation of Shadowgraphs With Other Data

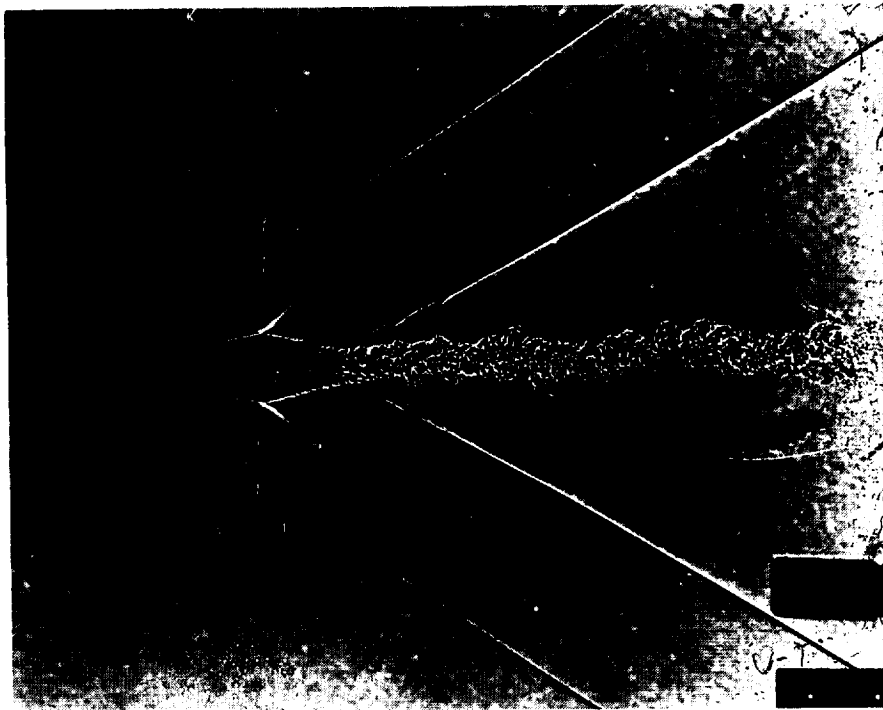
The strongly supportive nature of what is seen in shadowgraphs and what is measured with other techniques needs little additional emphasis. For example, it is evident that if a change in Reynolds number changes the base region from laminar to turbulent, a change in drag coefficient is to be expected. If the location of transition to turbulent flow changes from test to test under similar flight conditions, the skin friction coefficient and drag coefficient may show significant changes<sup>8,41</sup>. If two model flights exhibit considerably different flow separations near the stabilizer, then their stability coefficients will probably differ. If a shock wave comes near to a body surface above a given angle of attack, non-linearity of the aerodynamics may follow. The interplay and correlation of shadowgraph study with other measurement techniques in ballistic range testing is continual. It is one of the more powerful aspects of the use of ballistic ranges for study of aerodynamics and fluid mechanics.

#### REFERENCES

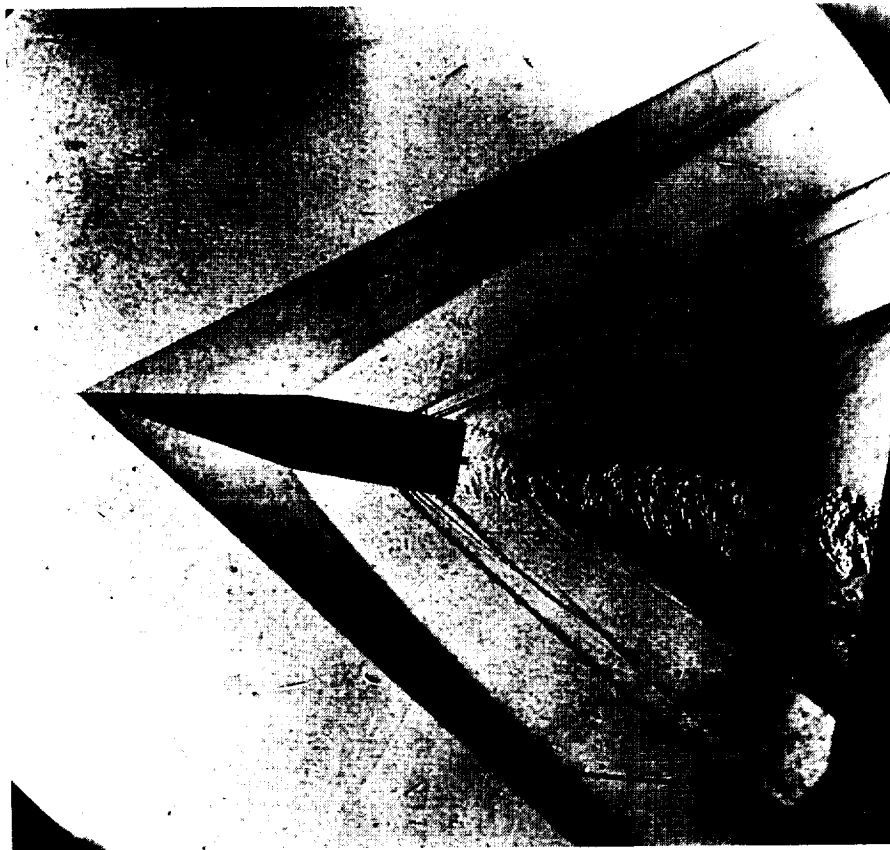
- 8.1 Mach, Ludwig      *Further Research on Projectiles*. Kaiserlichen Akademie der Wissenschaften, Wien, Sitzungsberichte, 1896, pp.605-633.
- 8.2 Boys, C.V.      *Photography of Flying Bullets*. Journal of Photographic Society of Great Britain, April, 1892.
- 8.3 Holder, D.W.  
North, R.J.  
Wood, G.P.      *Optical Methods for Examining the Flow in High-Speed Wind Tunnels*. Agardograph 23, November, 1956.
- 8.4 Seiff, A.  
Sommer, S.C.      *Experimental Investigation of the Drag of 30°, 60°, and 90° Cone Cylinders at Mach Numbers between 1.5 and 8.2*. NACA Research Memorandum RM A52A14b, 1952.
- 8.5 Keenan, P.C.  
Polachek, H.      *The Measurement of Densities in Shock Waves by the Shadowgraph Method*. NAVORD Report 86-46, 1946.
- 8.6 Strong, John      *Concepts of Classical Optics*. Published by W.H. Freeman and Co., 1958.
- 8.7 Briggs, R.O.  
Kerwin, W.J.  
Schmidt, S.F.      *Instrumentation of the Ames Supersonic Free-Flight Wind Tunnel*. NACA RM A52A18, April, 1952.
- 8.8 Slattery, R.E.  
Clay, W.G.      *Some Instrumentation Techniques Used at the Re-Entry Simulating Range*. International Congress on Instrumentation in Aerospace Simulation Facilities, September, 1964.
- 8.9 Zobel, T.      *Entwicklung und Bau eines Interferenzgerätes zur optischen Messung von Dichtefeldern*. Available in translation as NACA TM 1184, 1947.
- 8.10 Winkler, E.H.      *Analytical Studies of the Mach-Zehnder Interferometer*. Parts I and II, NOL Reports 1077 and 1099, U.S. Naval Ordnance Laboratory, 1950.
- 8.11 Bennett, F.D.      *Effect of Size and Spectral Purity of Source on Fringe Pattern of the Mach-Zehnder Interferometer*. BRL Report No.742, October, 1950; also in J.Appl. Phys.22, 776, 1951.
- 8.12 Sleator, D.B.  
Bergdolt, V.E.  
Bennett, F.D.      *Monochromatic Light Source for Interferometry of High-Speed Gas Flows*. BRL Memorandum Report 594, April, 1952.
- 8.13 Rowe, R.L.      *Interferometers for Hypervelocity Ranges*. Instrument Society of America Transactions. January, 1966.
- 8.14 Heflinger, L.O.  
Wuerker, R.F.  
Brooks, R.E.      *Holograph Interferometry*. J. Appl. Phys., Vol.37, No.2, February, 1966.

- 8.15 Seiff, A.  
Short, B.J. *An Investigation of Supersonic Turbulent Boundary Layers on Slender Bodies of Revolution in Free-Flight by Use of a Mach-Zehnder Interferometer and Shadowgraphs.* NACA TN 4364, September, 1958.
- 8.16 Ladenburg, R.  
Van Voorhis, C.C.  
Winckler, J. *Interferometric Study of Supersonic Phenomena.* NAVORD Report 69-46.
- 8.17 Sedney, R.  
Kahl, G.D. *Ballistic Missiles and Space Technology.* Pergamon Press, Vol.II, London, 1961, p.337.
- 8.18 Bradley, J.W.  
Oskey, V.  
Patchell, J.R. *An Interferometric Study of a  $\frac{1}{4}$  Inch Sphere at Mach 9.66 in Air.* BRL MR 1665, June, 1965.
- 8.19 Giese, J.H.  
Bergdolt, V.E. *Interferometric Studies of Supersonic Flows About Truncated Cones.* BRL R 830, September, 1952.
- 8.20 Spurk, J.H.  
Bartos, J.M. *Interferometric Measurement of the Nonequilibrium Flow Field Around a Cone.* BRL Report No.1333, August, 1966.
- 8.21 Seiff, A.  
Whiting, E.E. *Calculation of Flow Fields From Bow-Wave Profiles for the Down-stream Region of Blunt-Nosed Circular Cylinders in Axial Hypersonic Flight.* NASA TN D-1147, November, 1961.
- 8.22 Seiff, A.  
Whiting, E.E. *A Correlation Study of the Bow-Wave Profiles of Blunt Bodies.* NASA TN D-1148, February, 1962.
- 8.23 Seiff, A. *Recent Information on Hypersonic Flow Fields.* Gas Dynamics in Space Exploration, NASA SP-24, December, 1962.
- 8.24 Kirk, D.B.  
Chapman, G.T. *Free-Flight Tests of a Blunt-Nosed Flare-Stabilized Body at Speeds to 8.2 Km/Sec.* J. of Spacecraft and Rockets, Vol.3, No.3, March, 1966, p.374.
- 8.25 Seiff, A.  
Sommer, S.C.  
Canning, T.N. *Some Experiments at High Supersonic Speeds on the Aerodynamic and Boundary-Layer Transition Characteristics of High-Drag Bodies of Revolution.* NACA RM A56105, January, 1957.
- 8.26 Jedlicka, J.R.  
Wilkins, M.E.  
Seiff, A. *Experimental Determination of Boundary-Layer Transition on a Body of Revolution at  $M = 3.5$ .* NACA TN 3342, 1954.
- 8.27 James, C.S. *Observations of Turbulent-Burst Geometry and Growth in Supersonic Flow.* NACA TN 4235, April, 1958.
- 8.28 Charters, A.C.  
Turetsky, R.A. *Determination of Base Pressure From Free-Flight Data.* Ballistic Research Laboratory Report 653, March, 1948.
- 8.29 *Equations, Tables, and Charts for Compressible Flow.* Ames Research Staff, NACA Report 1135, 1953.
- 8.30 Murphy, C.H. *Growth of the Turbulent Wake Behind a Supersonic Sphere.* BRL Memo Rep.No.1388, February, 1962.
- 8.31 Slattery, R.E.  
Clay, W.G. *Physics of Fluids.* Vol.5, 1962, P.849.
- 8.32 Liepmann, H.W.  
Puckett, A.E. *Introduction to Aerodynamics of a Compressible Fluid.* Galcit Aeronautical Series, John Wiley and Sons, Inc., New York.
- 8.33 Schwartz, R.N.  
Eckerman, J. *Shock Location in Front of a Sphere as a Measure of Real Gas Effects.* NAVORD Rep. 3904, February, 1955.
- 8.34 Stephenson, J.D. *A Technique for Determining Relaxation Times by Free-Flight Tests of Low-Fineness-Ratio Cones, With Experimental Results in Air at Equilibrium Temperatures up to 3440° K.* NASA TN D-327, September, 1960.
- 8.35 Inouye, M. *Blunt Body Solutions for Spheres and Ellipsoids in Equilibrium Gas Mixtures.* NASA TN D-2780, May, 1965.
- 8.36 Wittliff, C.E.  
Curtis, J.T. *Normal Shock Wave Parameters in Equilibrium Air.* Cornell Aero. Lab. Rep. CAL-111, November, 1961.

- 8.37 Canning, T.N.  
Sommer, S.C. *Investigation of Boundary-Layer Transition on Flat-Faced Bodies of Revolution at High Supersonic Speeds.* NACA RM A57C25, June, 1957.
- 8.38 Kruse, R.L. *Transition and Flow Reattachment Behind an Apollo-Like Body at Mach Numbers to 9.* NASA TN D-4645, July, 1968.
- 8.39 Morkovin, M.V. *Note on the Assessment of Flow Disturbances at a Blunt Body Traveling at Supersonic Speeds Owing to Flow Disturbances in Free Stream.* Paper No. 60, APM-10, J. Appl. Mechanics.
- 8.40 Page, W.A. *A Survey of Thermal Radiation Studies of Ablating Bodies in the Ballistic Range.* NASA TN D-3741, February, 1967.
- 8.41 Carros, R.J.  
James, C.S. *Some New Drag Data on the NACA RM-10 Missile and a Correlation of the Existing Drag Measurements at  $M = 1.6$  and  $3.0$ .* NACA TN 3171, June, 1954.

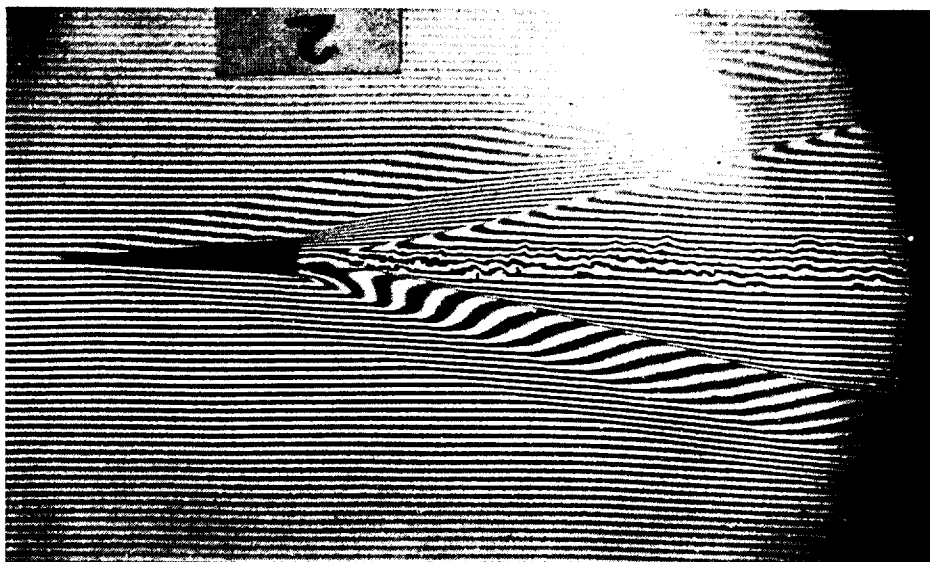


(a) Shadowgraph,  $M = 2$ , cone half-angle,  $9.5^\circ$



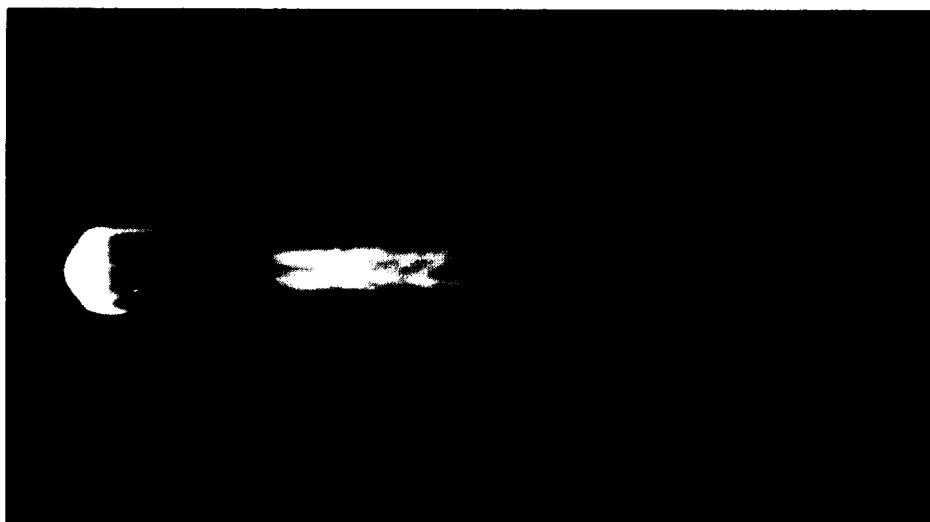
(b) Schlieren,  $M = 1.8$ , cone half-angle,  $9.5^\circ$ , knife edge vertical. (Courtesy of US Army Ballistic Research Laboratory)



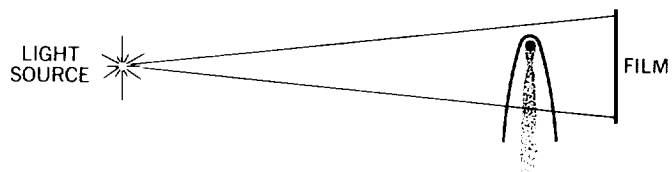


(c) Interferogram,  $M = 3.6$ , cone half-angle,  $4.1^\circ$

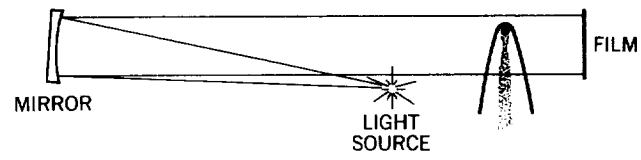
8.1 Representative shadowgraph, schlieren, and interferometer pictures of cones.



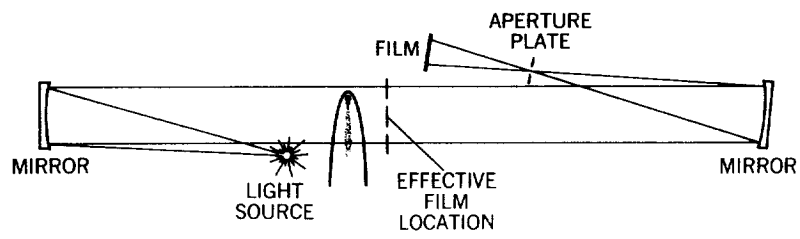
8.2 Self-luminous photograph of an ablating polycarbonate round-nosed, large-angle cone at a velocity of 7 km/sec, ambient density of 0.066 atmospheres



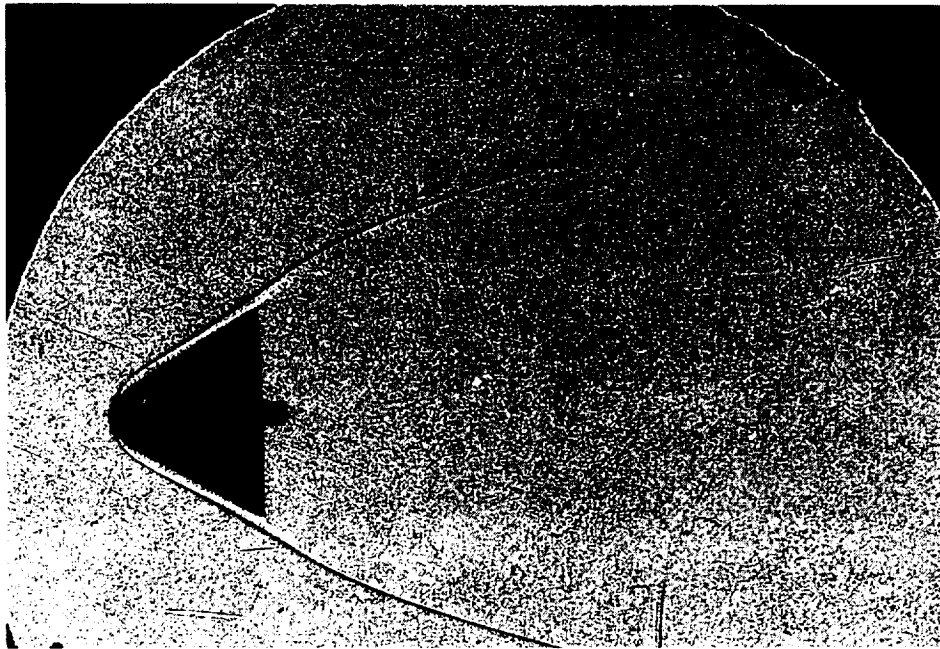
8.3 Conical-light-field shadowgraph



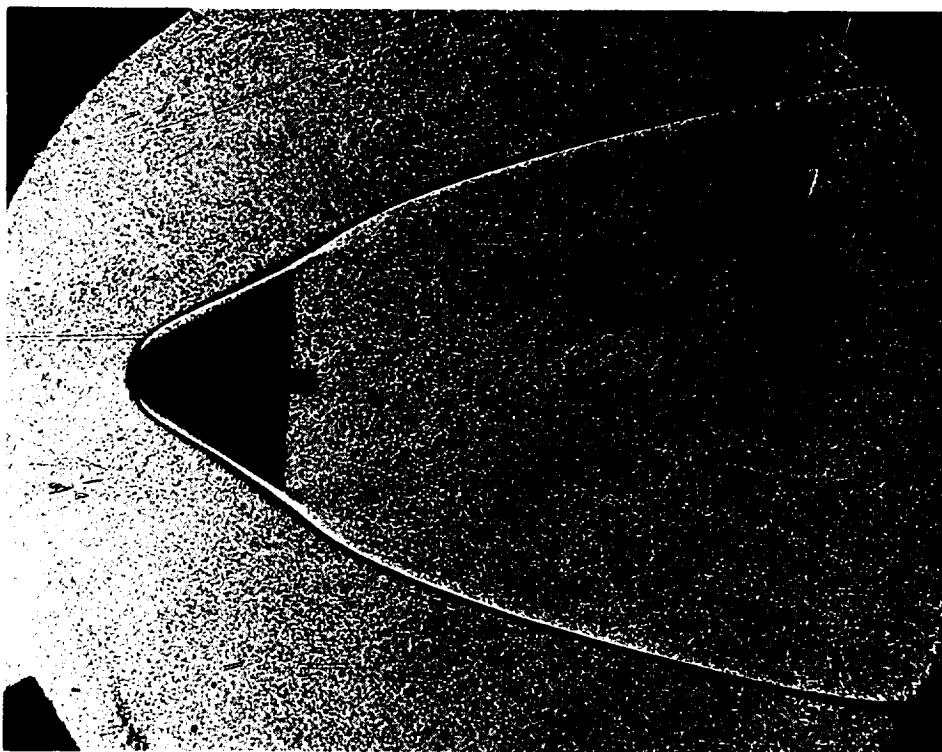
8.4 Parallel-light shadowgraph



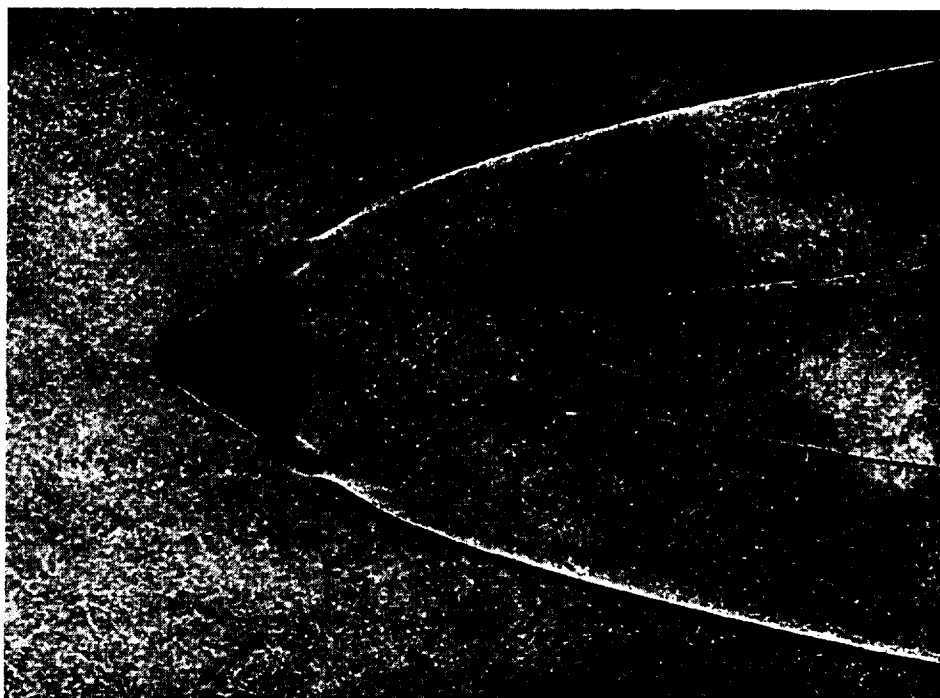
8.5 Focused shadowgraph



(a) Focused shadowgraph, low sensitivity

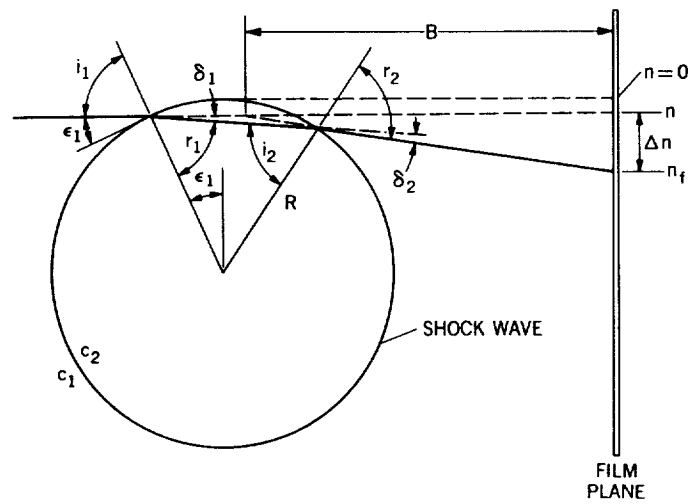


(b) Focused shadowgraph, intermediate sensitivity

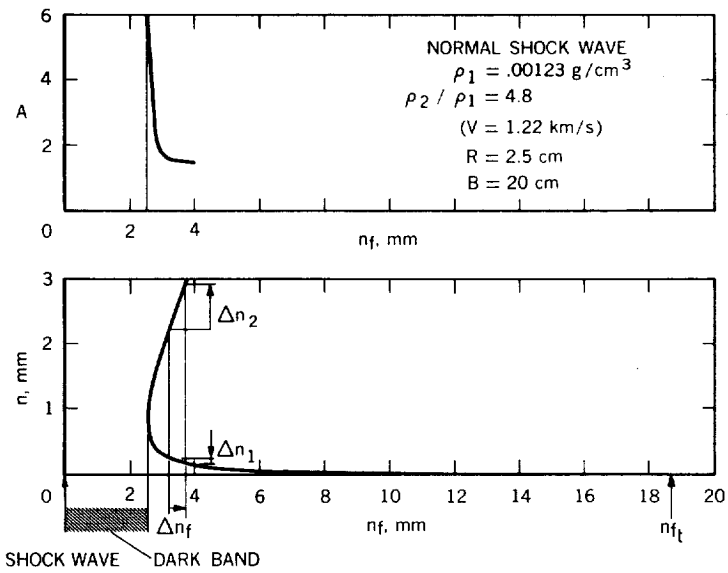


(c) Parallel-light shadowgraph (Figure 8.4), high sensitivity

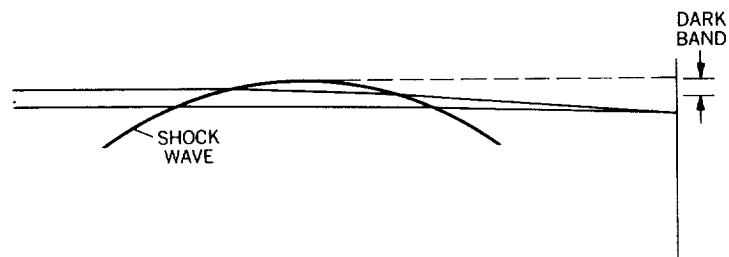
8.6 Shadowgraph pictures of a round-nosed  $30^\circ$  half-angle cone with various sensitivity settings



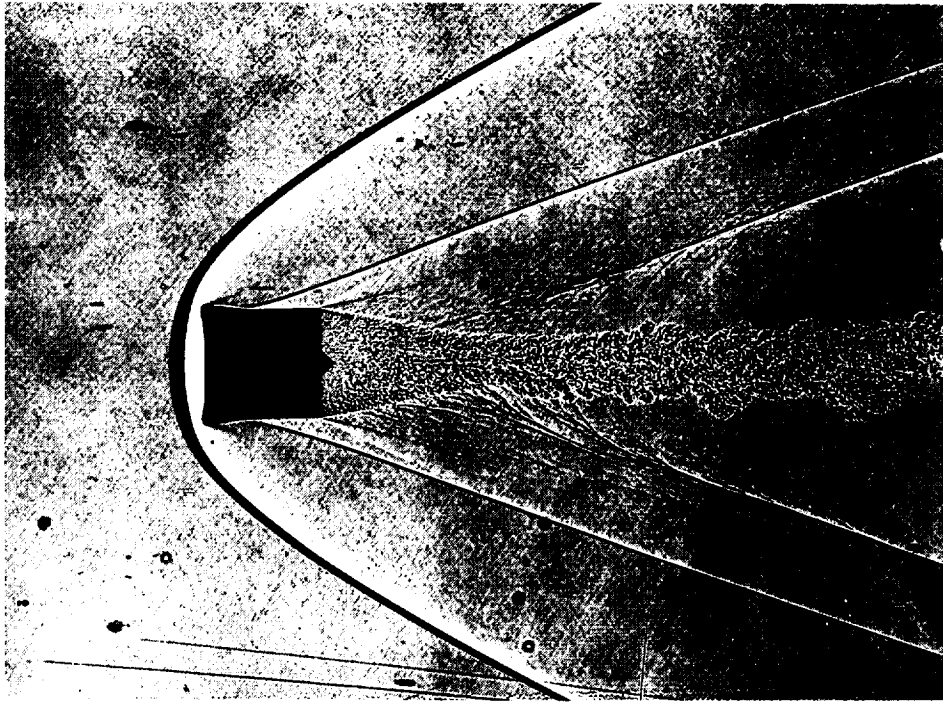
8.7 Light-ray deflections at a shock wave



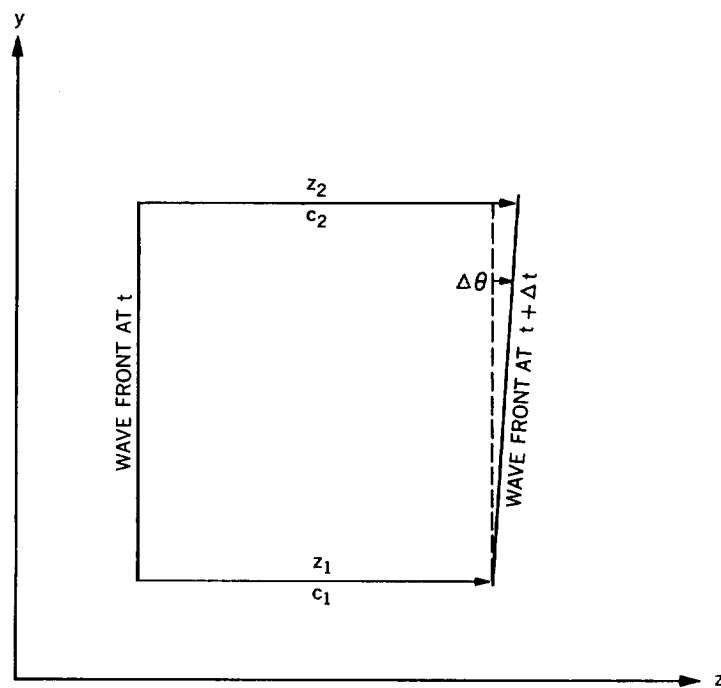
8.8 Example calculation of light-ray deflection at a shock wave, and light-amplification factors in the bright band



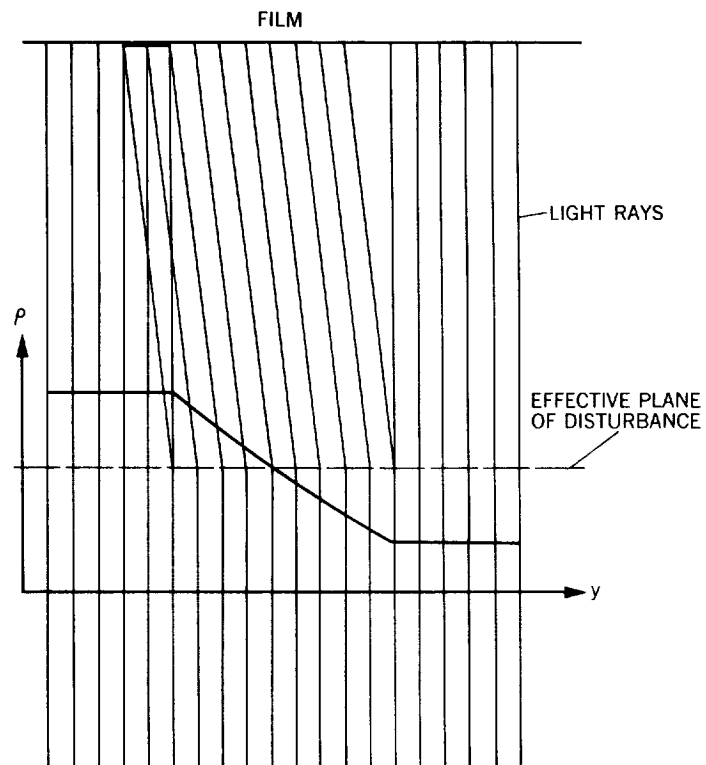
8.9 Two rays intersecting film at a common point



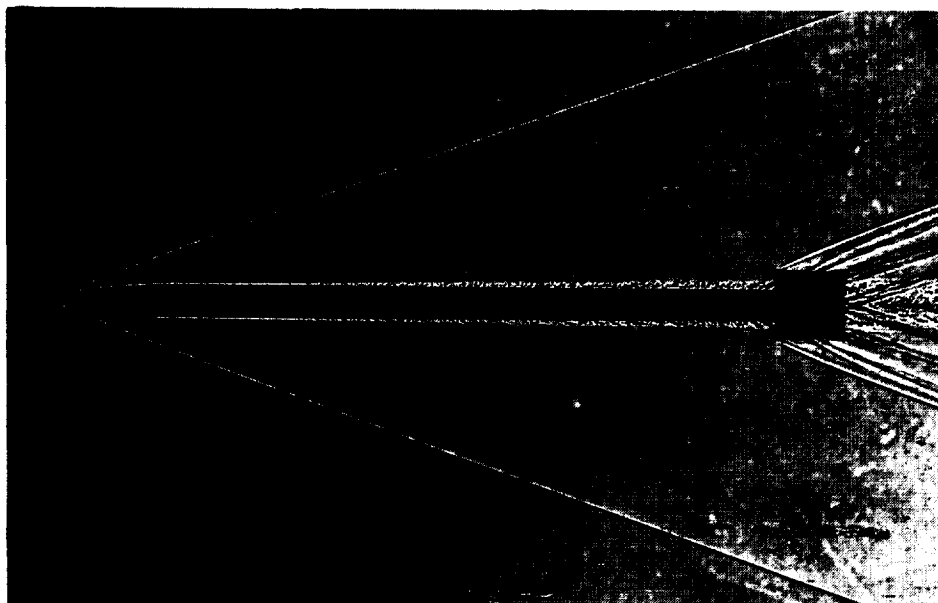
8.10 Shadowgraph showing shock-wave dark band width for conditions: velocity, 0.9 km/sec; 1-atm. ambient pressure; shock wave radius of curvature on axis of symmetry, 3.5 cm; and distance B from model to film approximately 30 cm



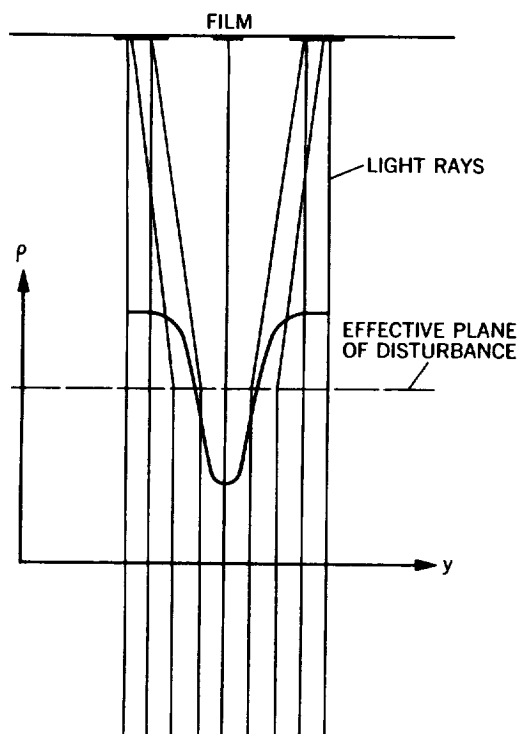
8.11 Wave-front rotation due to non-uniform light velocity



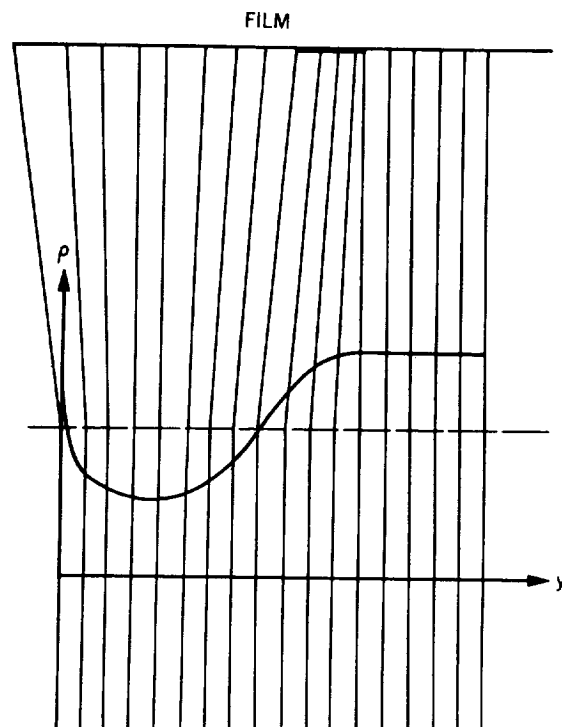
8.12 Schematic light ray paths in a Prandtl-Meyer expansion



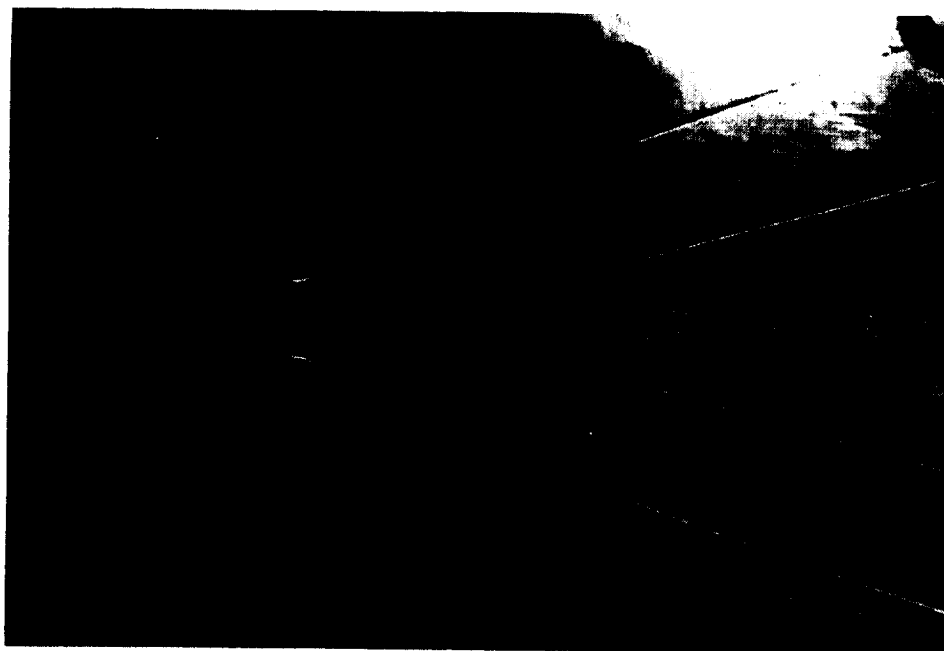
8.13 Shadowgraph of a turbulent boundary layer on a slender body of revolution at  $M = 3.5$ , length Reynolds number of 12 million

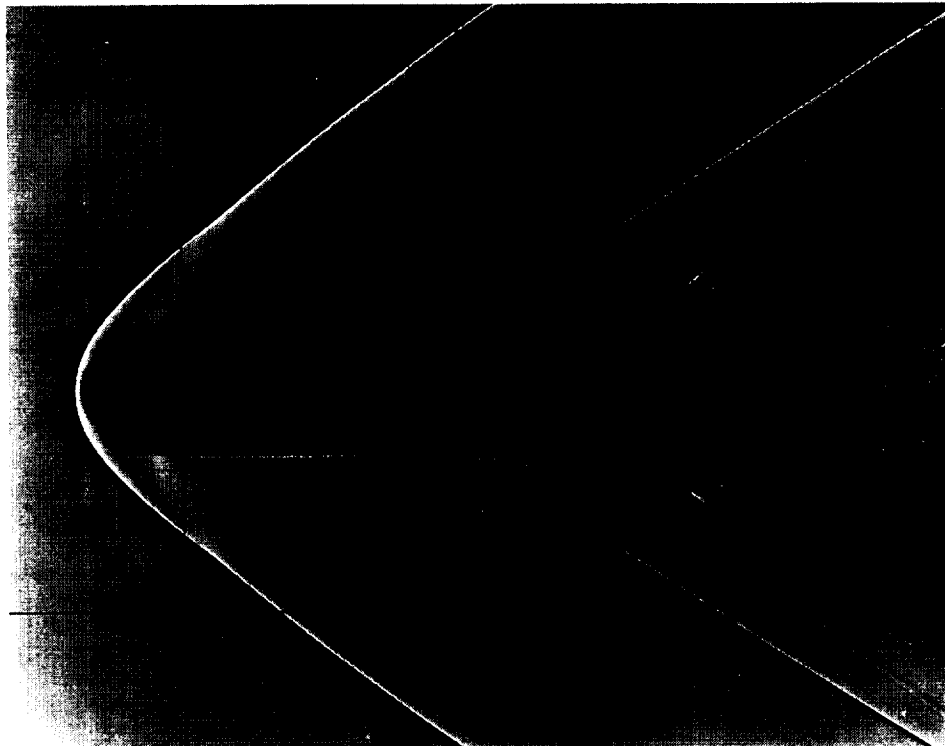


8.14 Light-ray paths in a turbulent eddy

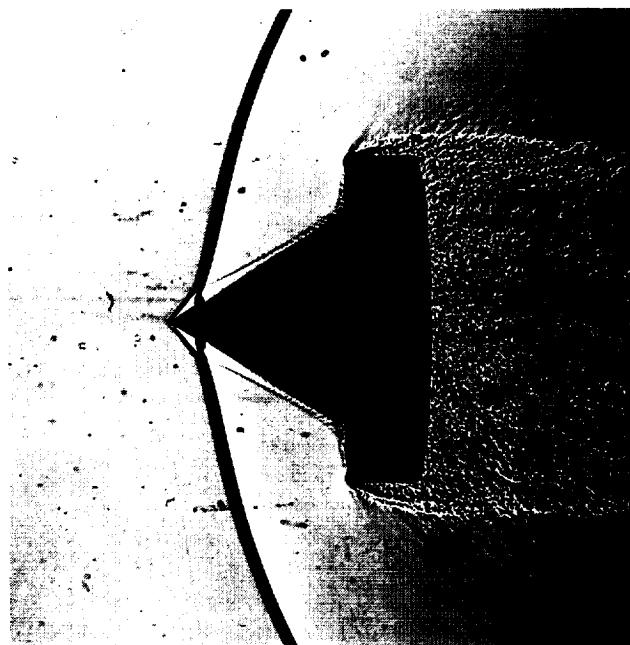


8.15 Light-ray paths in a cold-wall laminar boundary layer

8.16 Shadowgraph of 9.5°-half-angle cone at  $M = 4$ , showing separated laminar boundary-layer image behind base

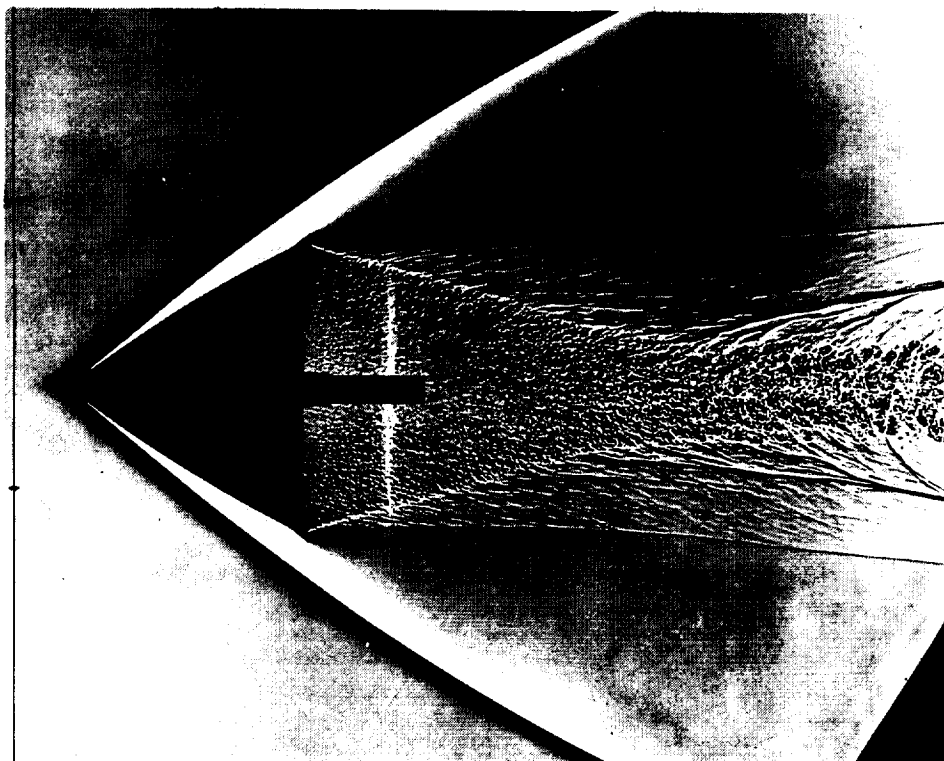


8.17 Line image in sublayer of a turbulent boundary layer behind the base of a flare-stabilized body  
( $M = 2.06$  ,  $Re = 6 \times 10^6$ )

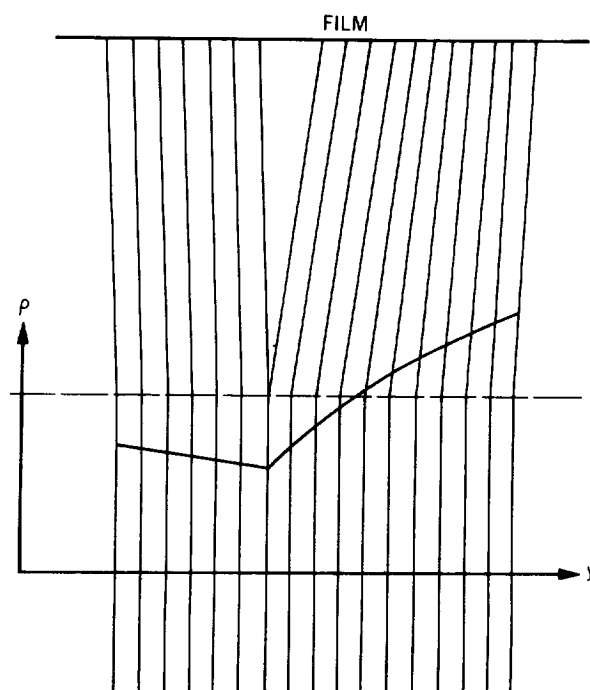


8.18 Image of a velocity-discontinuity streamline emanating from an intersection of shock waves

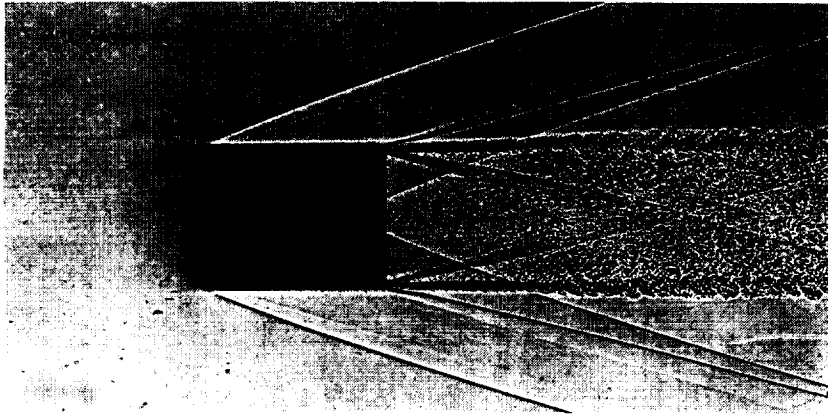




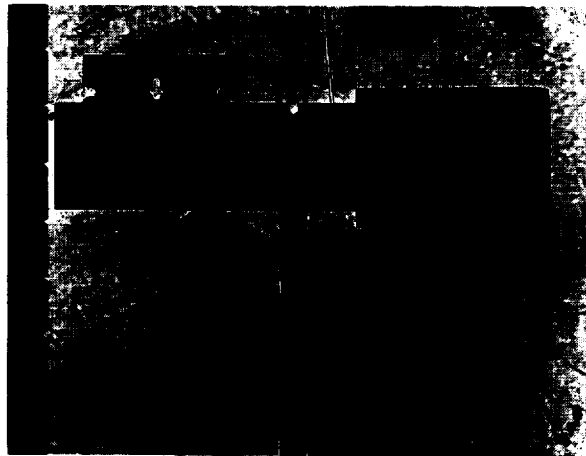
8.19 Marked streamlines, due to minute waves from body-fixed disturbances intersecting the bow wave



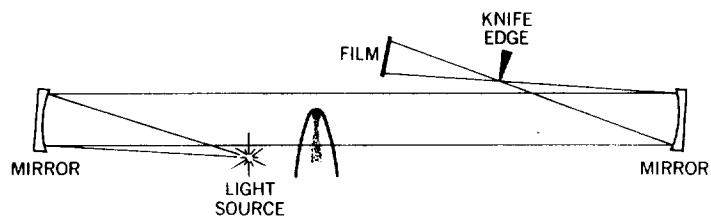
8.20 Light refraction at a streamline where density gradient is discontinuous



8.21 Shadowgraph of thin-walled tubular model with thick, turbulent boundary layer at  $M = 3.8$ , length Reynolds number of  $4 \times 10^6$



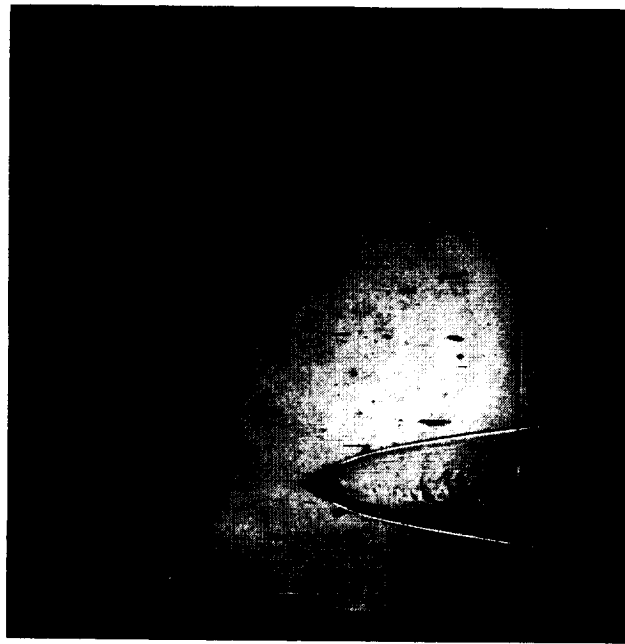
8.22 Diffraction fringes at the edges of a razor blade (left), thin-walled tubular model with serrated leading edge (right), and metal stand in a parallel-light shadowgraph system



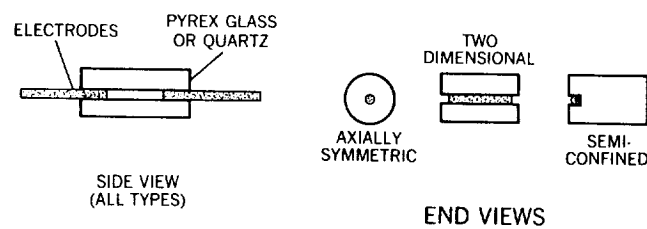
8.23 Parallel-light schlieren system



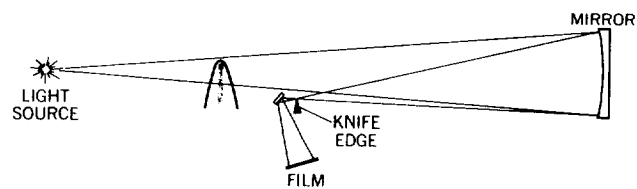
8.24 Shape variations of luminous region in a mercury-arc lamp (BH-6) when pulsed repeatedly at intervals of 10 microseconds



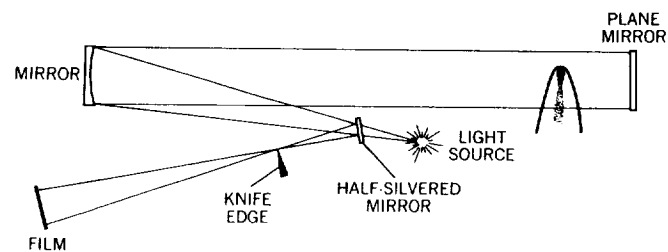
8.25 Schlieren effect obtained inadvertently in a focused shadowgraph system. Model,  $30^\circ$ -half-angle cone at a velocity of 6 km/sec, ambient pressure, 100 mm mercury



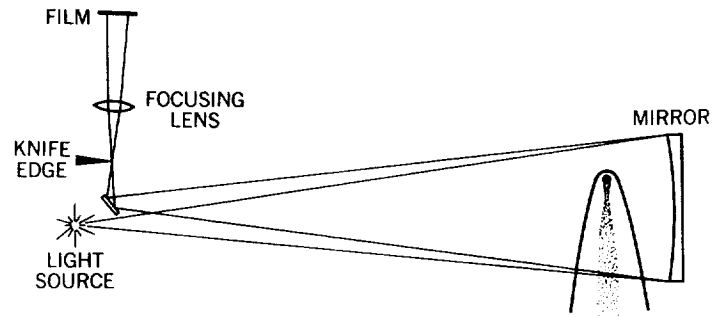
8.26 Sketches of confined spark gaps



8.27 Single-mirror, single-pass schlieren system



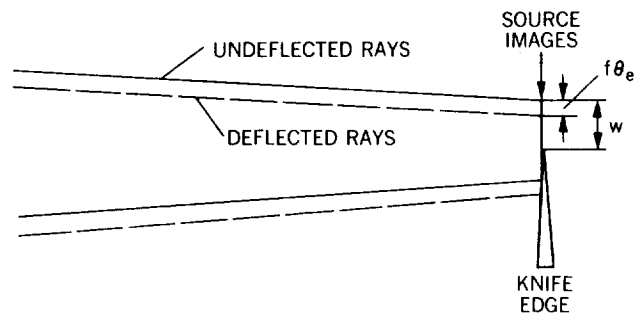
8.28 Double-pass, parallel-light schlieren system



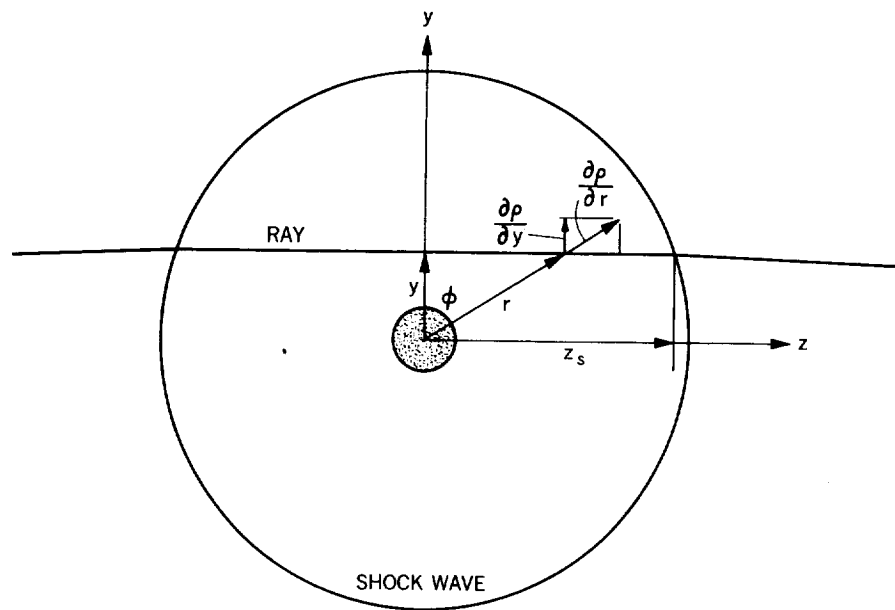
8.29 Double-pass, conical-light schlieren system



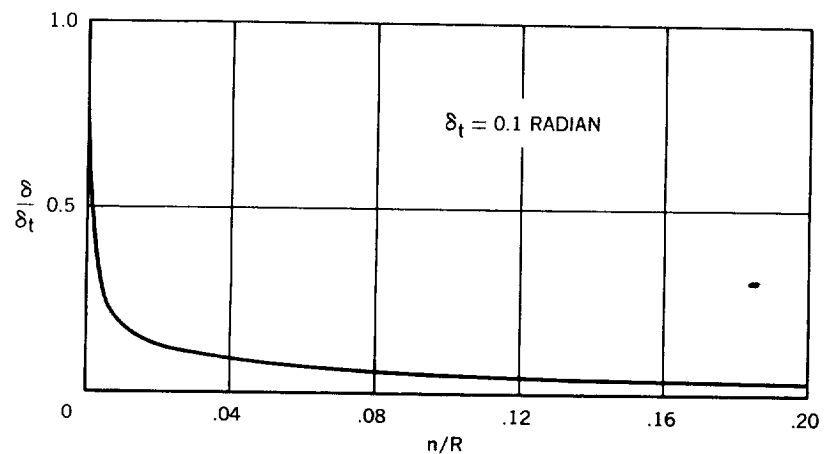
8.30 Schlieren photograph of a laminar wake at 0.013 atm. ambient pressure, undergoing initial stages of transition to turbulence. Model is a 12½°-half-angle cone at velocity of 2.4 km/sec



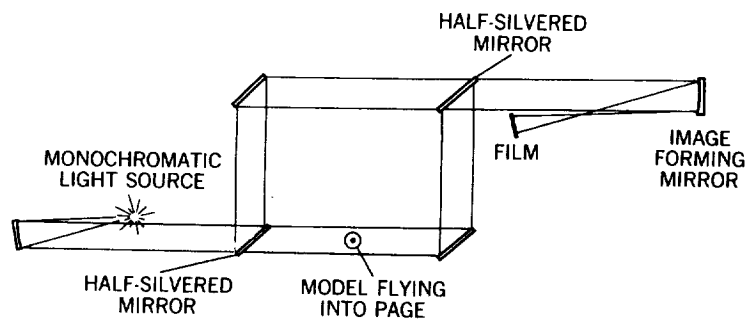
8.31 Action of the knife edge to differentially occult source images from various points in the flow field



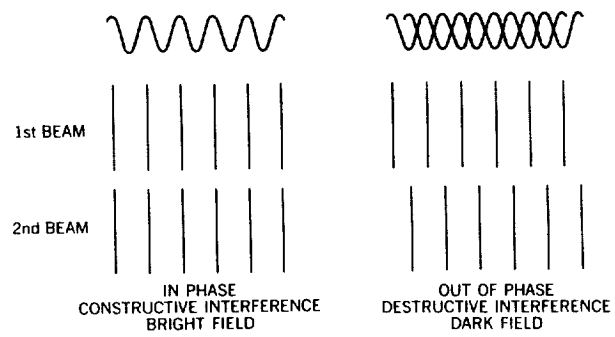
8.32 Notation for integrating Equation (8.26)



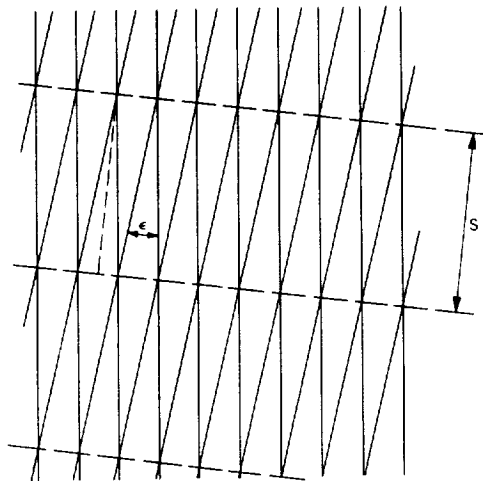
8.33 Relative deflections of rays passing through a shock wave as a function of normal distance from the tangent ray



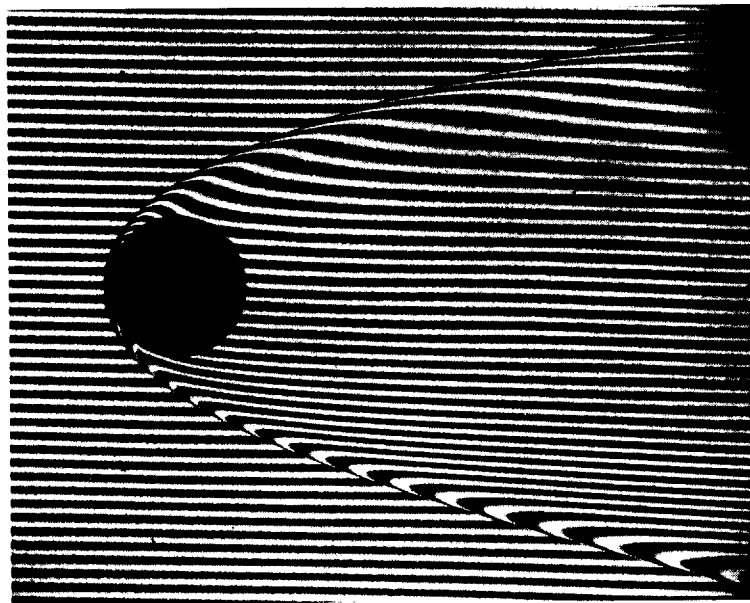
8.34 Optical arrangement, Mach-Zehnder interferometer



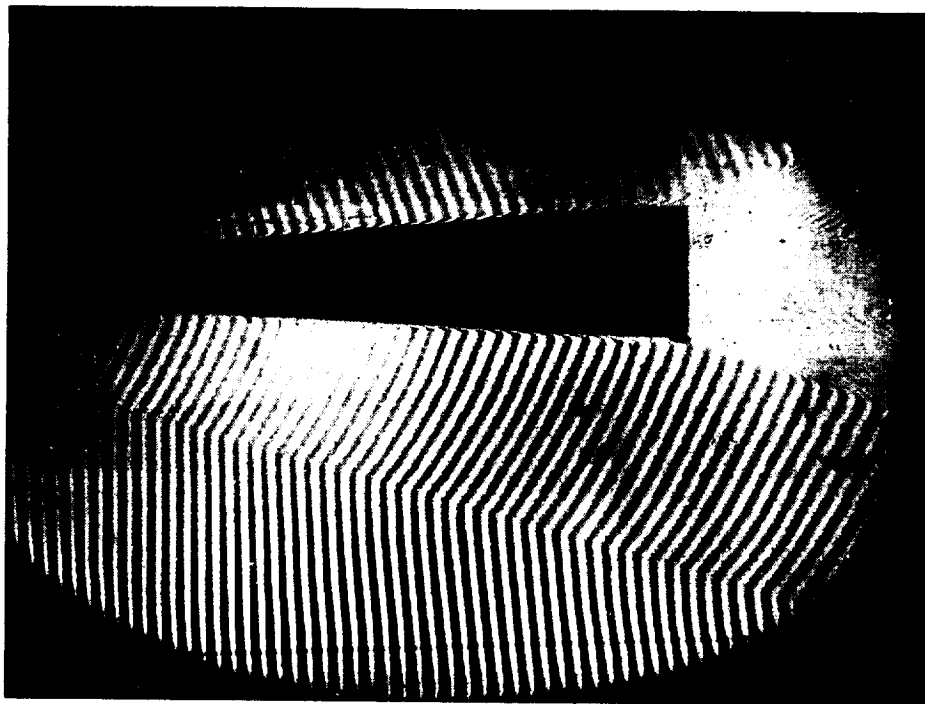
8.35 Interference between perfectly-parallel plane-wave trains



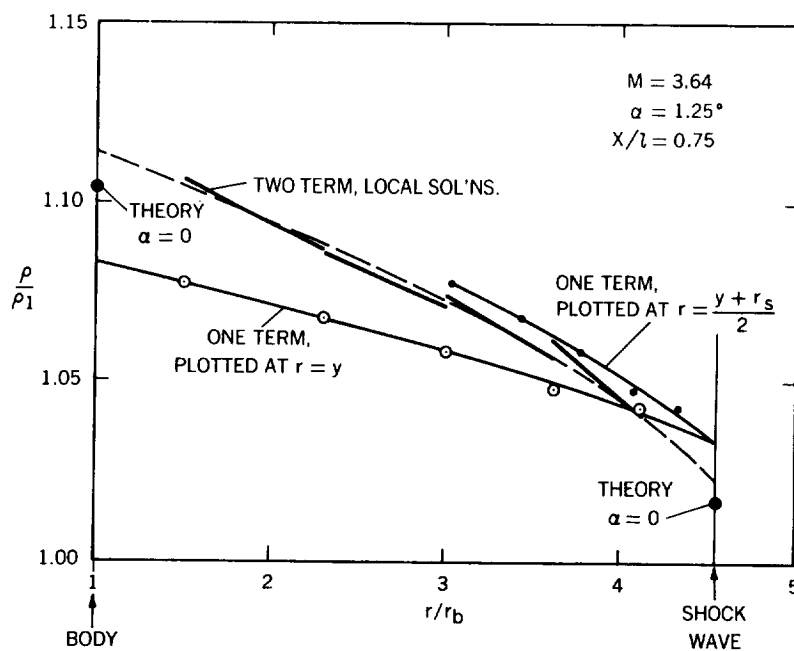
8.36 Interference between slightly inclined systems of plane waves



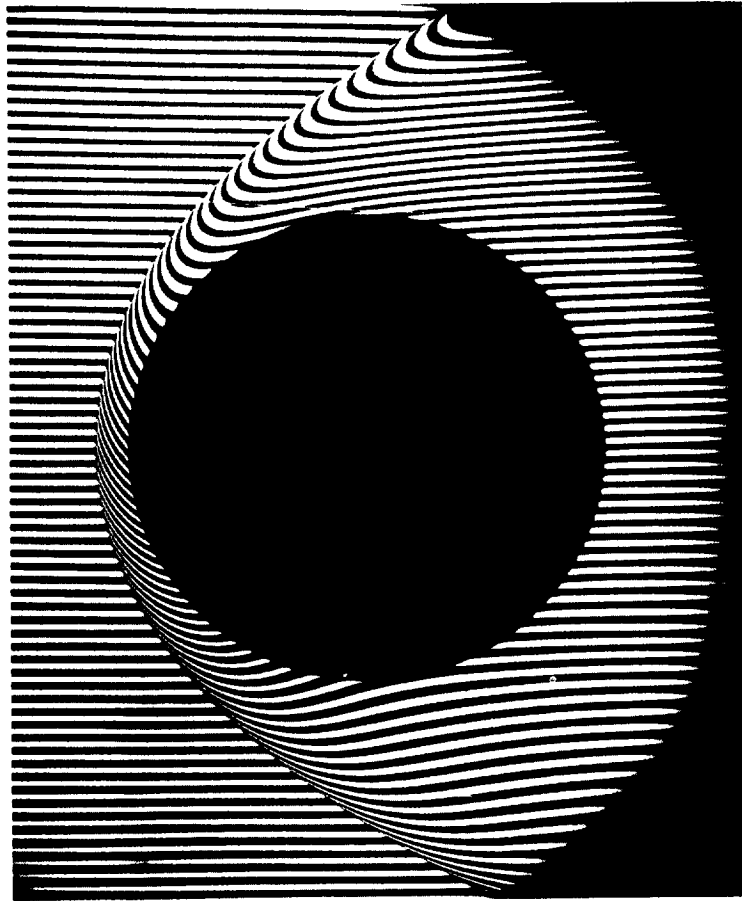
8.37 Interferogram of an aluminum sphere, 20 mm in diameter, at a velocity of 3.4 km/sec, range pressure of 0.1 atmosphere. (Courtesy of US Army Ballistic Research Laboratory)



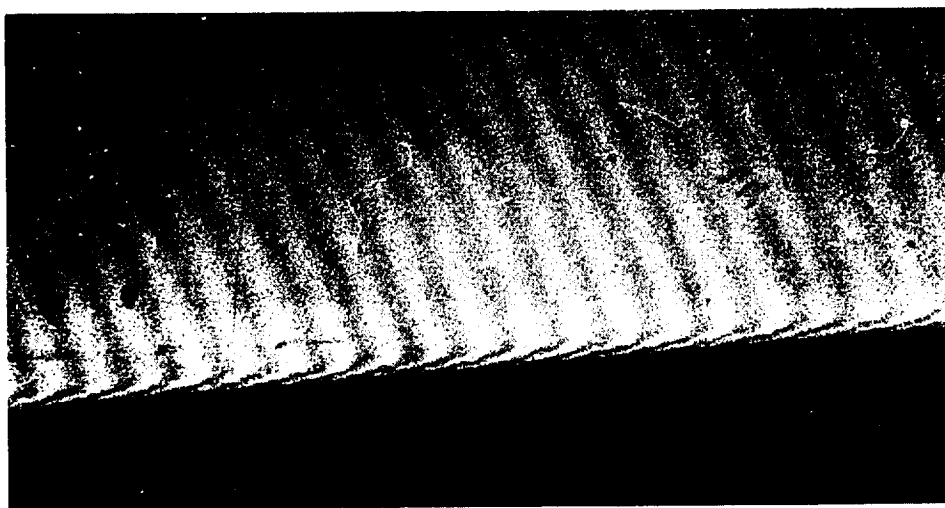
8.38 Interferogram of a cone in flight at 1.25 km/sec through air at one atmosphere pressure. Cone half-angle,  $3.58^\circ$ , and length, 30.5 cm



8.39 Density distributions, reduced by one-term and two-term series approximations from the interferogram of Figure (8.38)

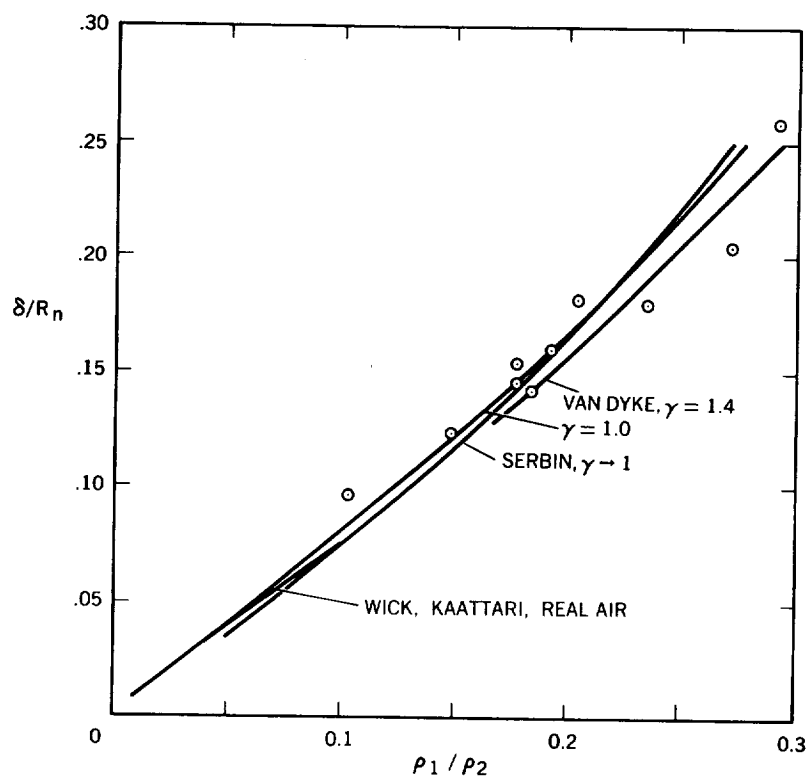


8.40 Interferogram of 8.9 cm-diameter sphere in flight at a Mach number of 5.7, range pressure of 0.05 atmospheres. (Courtesy of US Army Ballistic Research Laboratory)

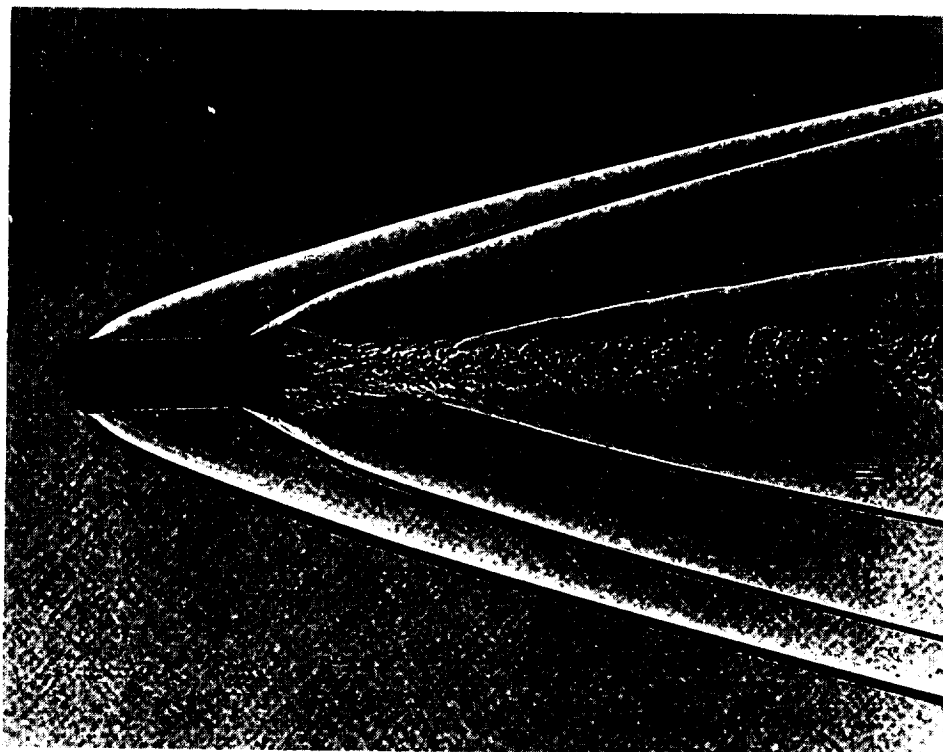


8.41 Enlargement of the fringes in the turbulent boundary layer along one edge of the model in Figure (8.38).  
Boundary-layer thickness, 2 mm; Reynolds number,  $25 \times 10^6$

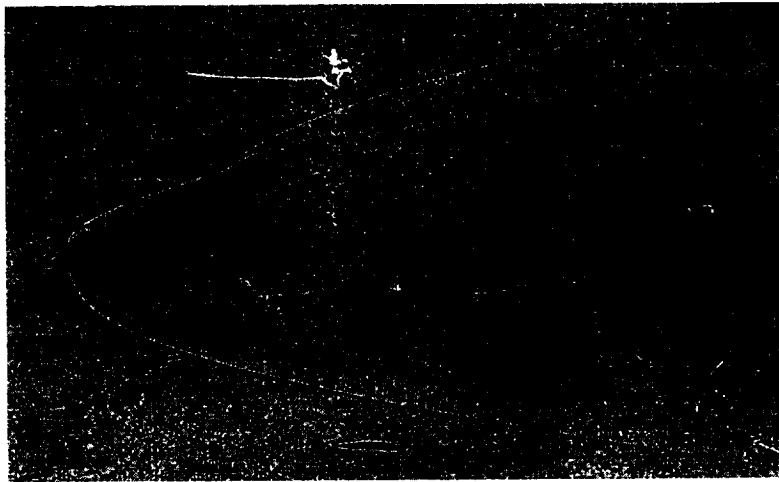




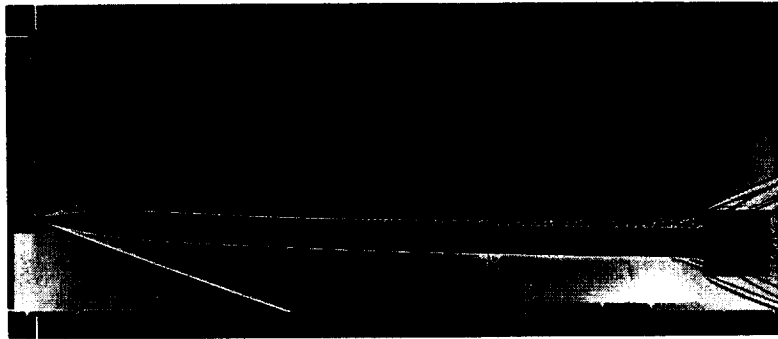
8.42 Comparison with theory of sphere shock-wave stand-off distances measured from shadowgraphs



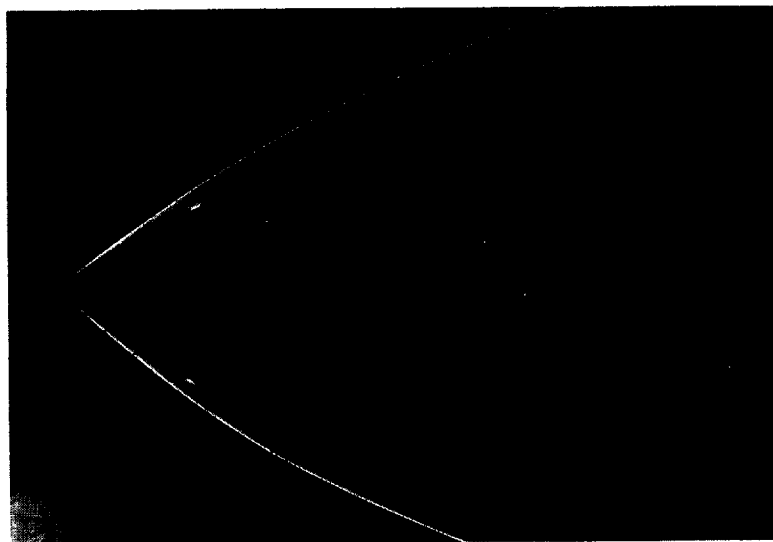
8.43 Shadowgraph of a flare-stabilized body in flight at a Mach number of 5.2, showing the oblique secondary shock wave generated by the flare



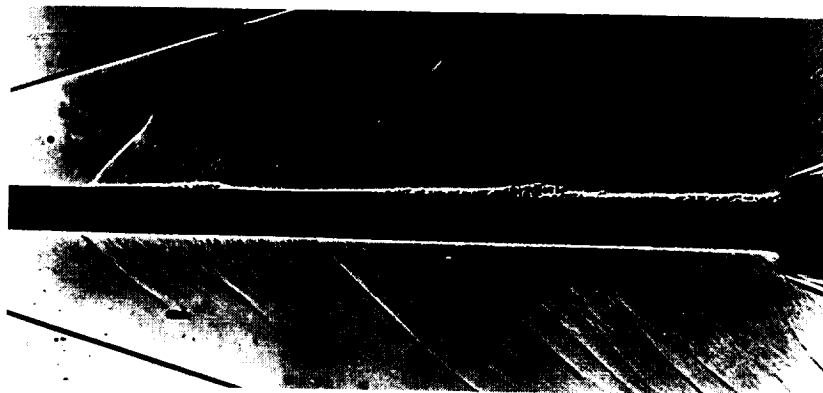
8.44 Interaction of the bow wave with the embedded shock wave from a downstream surface at a Mach number of 11,  $18^\circ$  angle of attack



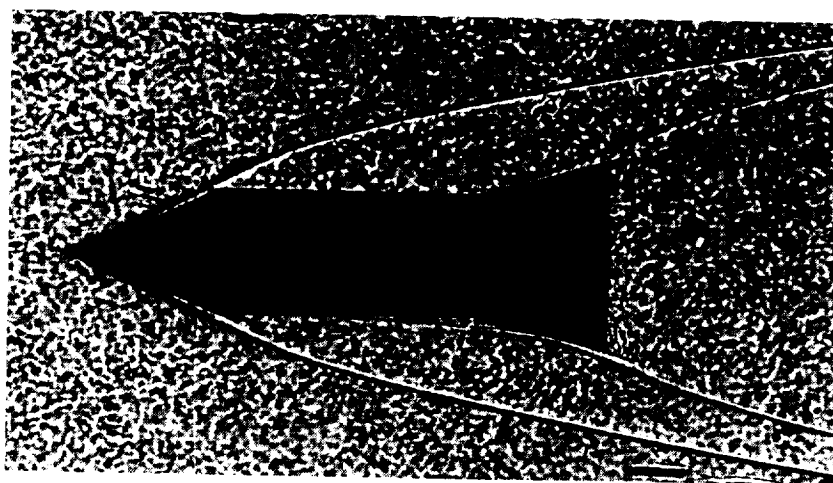
8.45 Acoustic field associated with boundary-layer turbulence on a slender body of revolution at a Mach number of 3.5



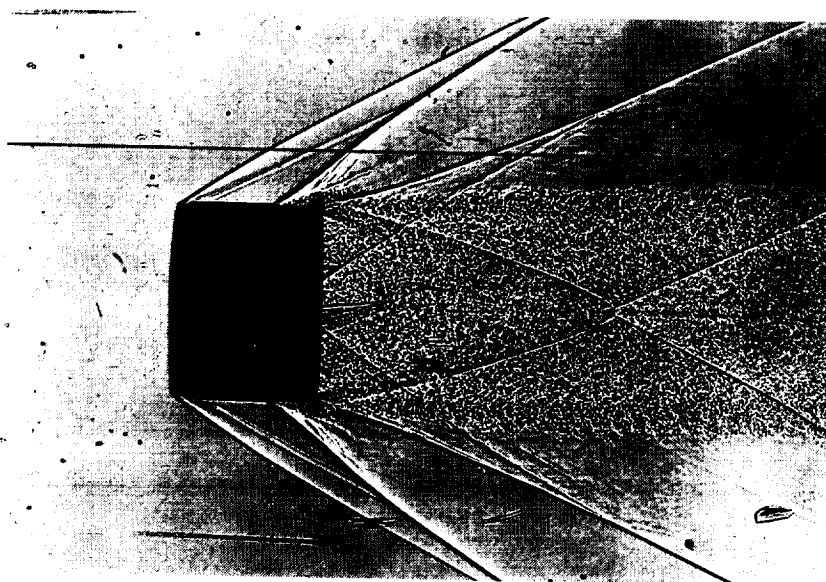
8.46 "Hairy" image at the model edge signifying the presence of turbulent boundary layer. Mach number 4; Reynolds number based on diameter,  $3.8 \times 10^6$



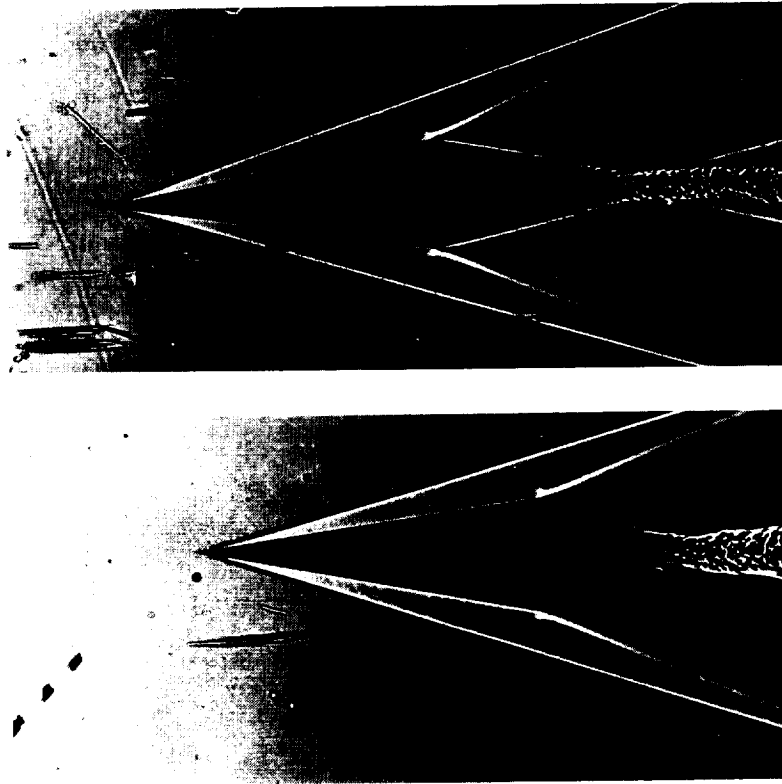
8.47 Shadowgraph of isolated bursts of turbulence on a slender body of revolution at a Mach number of 3.5



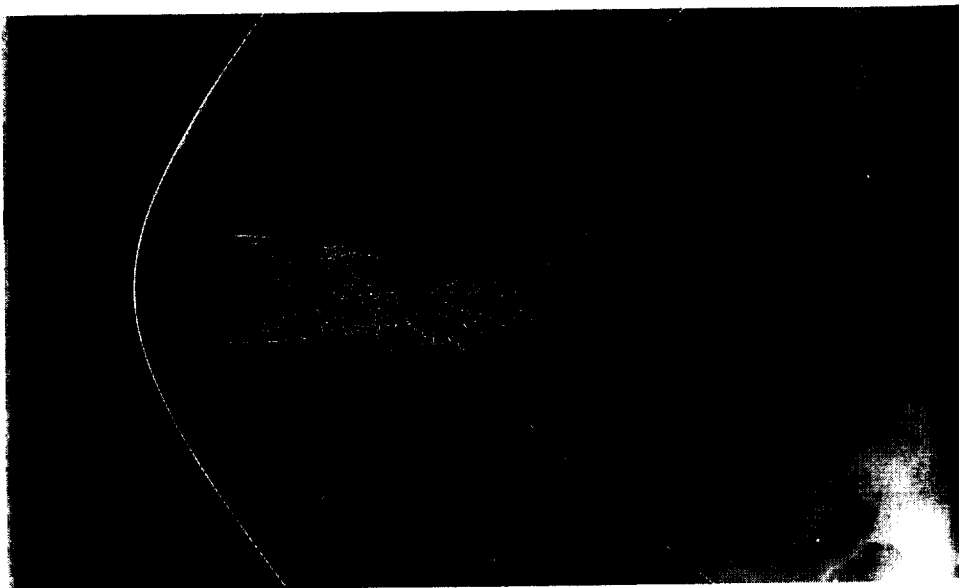
8.48 Laminar separation ahead of the flare on a flare-stabilized body at a Mach number of 15



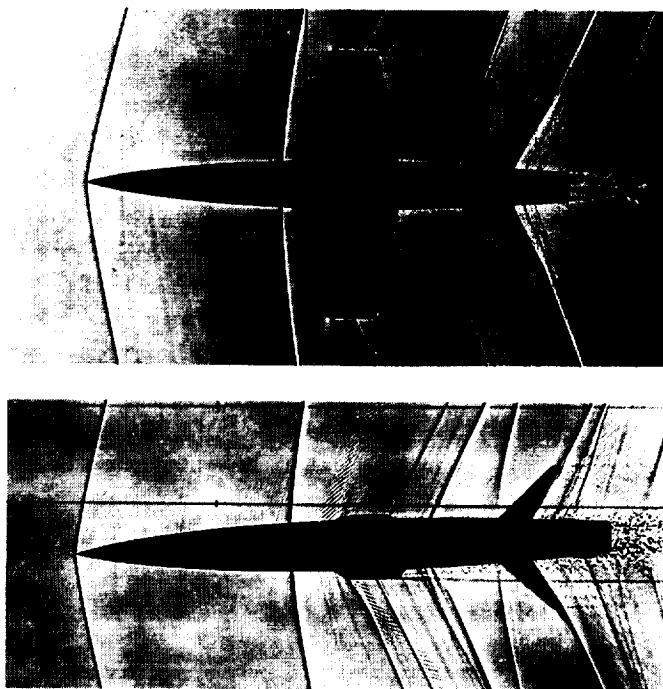
8.49 Turbulent separation in front of a step on a hollow-cylindrical model in flight at a Mach number of 2.2



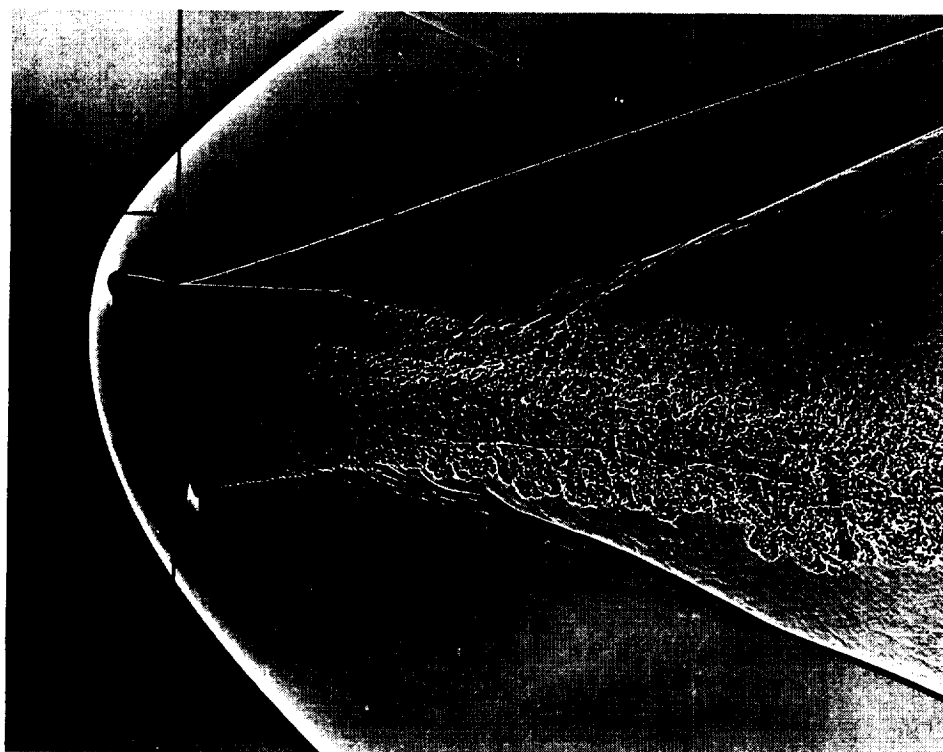
8.50 Illustration of the influence of laminar-turbulent transition on length of the base-flow region and thickness of the wake neck



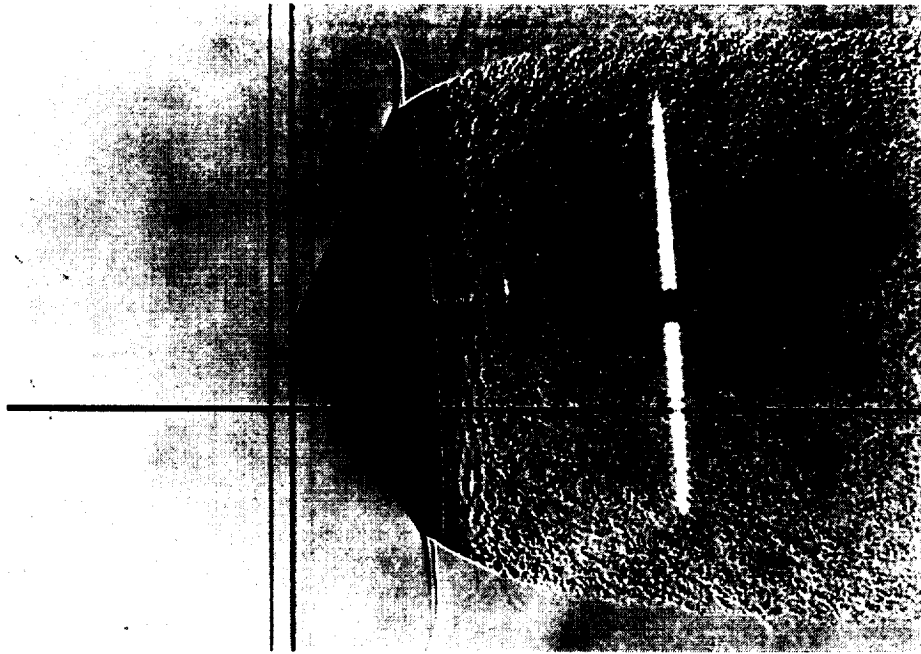
8.51 Field of Mach waves generated by body-fixed disturbances on a sphere between the sonic point and separation point at a flight Mach number of 1.4



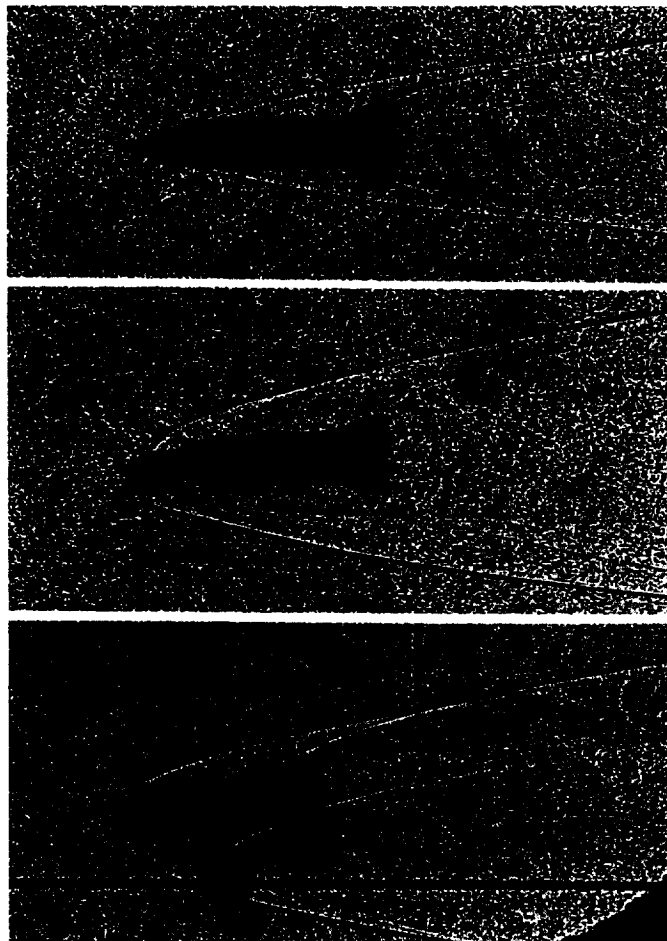
8.52 Field of high-frequency sound waves generated by shallow V grooves parallel to wing leading edge of an airplane model in flight at a low-supersonic Mach number (orthogonal views)



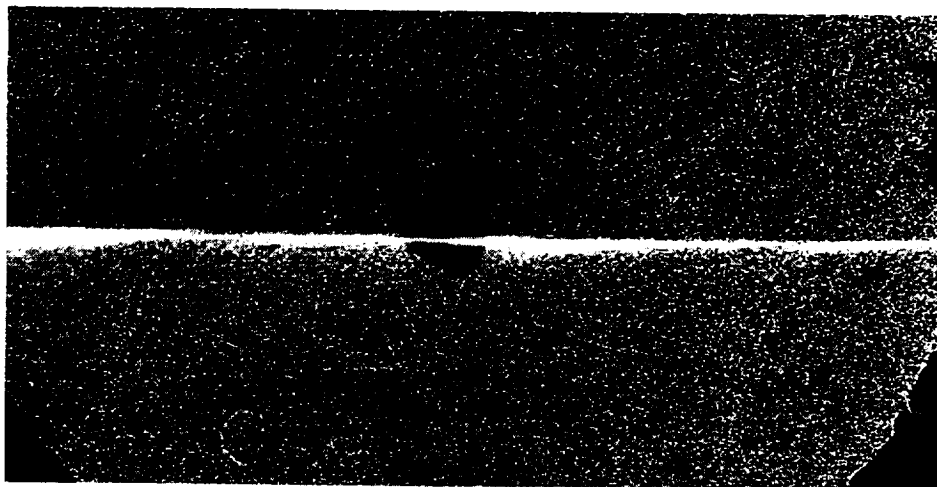
8.53 Oscillations in the stagnation region of a blunt-body flow at Mach number of 2.31, Reynolds number of  $1.6 \times 10^6$



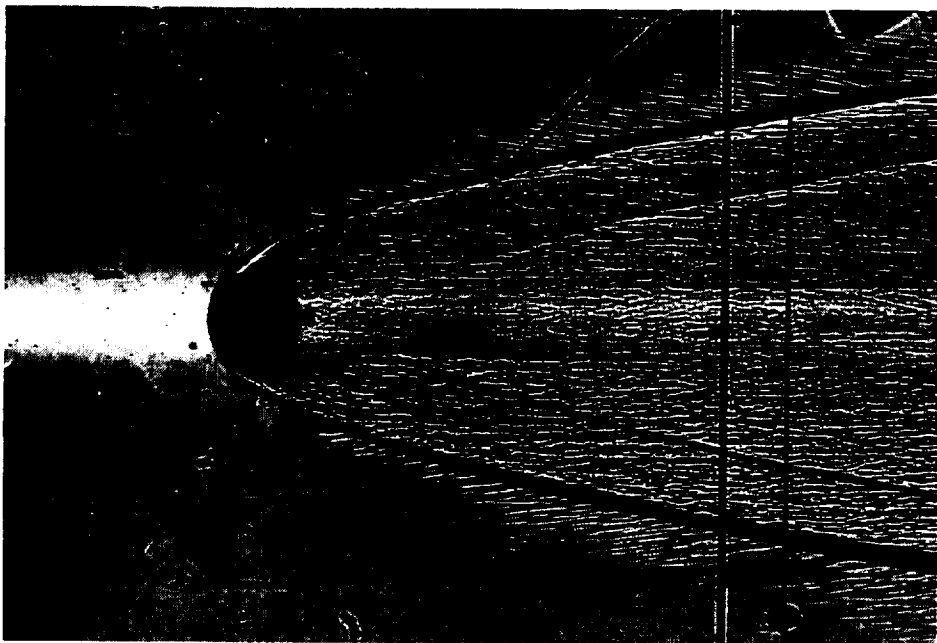
8.54 Transition effected by vortices transverse to the flow



8.55 Successive views of a model being separated into its component parts by drag forces in flight



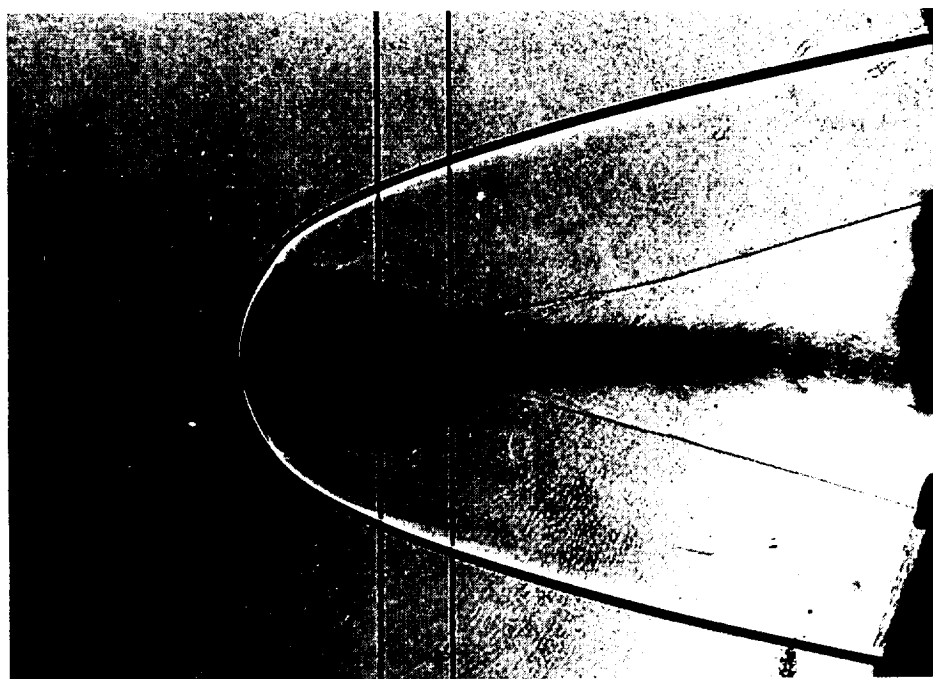
8.56 Model with titanium nose, burning chemically in flight at a velocity of 3 km/sec ( $M = 15$ )



8.57 Sintered iron-tungsten nose undergoing surface spalling and ejecting small particles due to intense surface heat transfer at a velocity of 4 km/sec in atmospheric air



8.58 Plastic model in violent ablation at a relative velocity of 12 km/sec



8.59 Shadowgraph of soot in the wake of an ablating polycarbonate model at a velocity of 5.8 km/sec and ambient pressure of 0.19 atm